HHS Public Access

Author manuscript

Neuron. Author manuscript; available in PMC 2020 September 04.

Published in final edited form as:

Neuron. 2019 September 04; 103(5): 820–835.e7. doi:10.1016/j.neuron.2019.06.010.

TREM2 Acts Downstream of CD33 in Modulating Microglial Pathology in Alzheimer's Disease

Ana Griciuc[1], **Shaun Patel**[1], **Anthony N. Federico**[1], **Se Hoon Choi**[1], **Brendan J. Innes**[1], **Mary K. Oram**[1], **Gea Cereghetti**[1,2], **Danielle McGinty**[1], **Anthony Anselmo**[3], **Ruslan I. Sadreyev**[3], **Suzanne E. Hickman**[4], **Joseph El Khoury**[4], **Marco Colonna**[5], **Rudolph E. Tanzi**[1,6,*]

[1]Genetics and Aging Research Unit, Department of Neurology, Massachusetts General Hospital and Harvard Medical School, Charlestown, MA 02129, USA [2]Institute of Biochemistry, Department of Biology, ETH Zürich, 8093 Zürich, Switzerland [3]Department of Molecular Biology, Massachusetts General Hospital and Harvard Medical School, Boston, MA 02114, USA [4]Center for Immunology and Inflammatory Diseases, Massachusetts General Hospital and Harvard Medical School, Charlestown, MA 02129, USA [5]Department of Pathology and Immunology, Washington University School of Medicine, St. Louis, MO 63110, USA [6]Lead contact: Rudolph E. Tanzi, Genetics and Aging Research Unit, Department of Neurology, Massachusetts General Hospital and Harvard Medical School. 114 16th Street, Charlestown, MA 02129, USA. phone: 617-726-6845, fax: 617-724-1823

Summary

The microglial receptors, CD33 and TREM2, have been associated with risk for Alzheimer's disease (AD). Here, we investigated crosstalk between CD33 and TREM2. We showed that knock-out of *CD33* attenuated amyloid beta (Aβ) pathology and improved cognition in *5xFAD* mice, both of which were abrogated by additional *TREM2* knock-out. Knocking out *TREM2* in *5xFAD* mice exacerbated Aβ pathology and neurodegeneration, but reduced Iba1^{+} cell numbers, all of which could not be rescued by additional *CD33* knock-out. RNA-seq profiling of microglia revealed that genes related to phagocytosis and signaling (IL-6, IL-8, acute phase response) are upregulated in *5xFAD;CD33*$^{-/-}$ and downregulated in *5xFAD;TREM2*$^{-/-}$ mice. Differential gene expression in *5xFAD;CD33*$^{-/-}$ microglia depended on the presence of *TREM2*, suggesting TREM2 acts downstream of CD33. Crosstalk between CD33 and TREM2 includes regulation of

*Correspondence: tanzi@helix.mgh.harvard.edu.

Author Contributions

Conceptualization, A.G. and R.E.T.; Methodology, A.G., S.P., S.E.H., J.E.K., M.C., and R.E.T.; Software, S.P., A.N.F., A.A., and R.I.S.; Formal Analysis, Data Curation: A.G., S.P., A.N.F., and A.A; Investigation, A.G., A.N.F., S.H.C., B.J.I., M.K.O., G.C., and D.M.; Resources: R.I.S. and M.C.; Writing - Original, A.G. and R.E.T.; Writing - Review and Editing, A.G., S.P., S.H.C., R.I.S., S.E.H., J.E.K., M.C., and R.E.T.; Visualization, A.G., S.P., A.N.F., S.H.C., and R.E.T.; Supervision, R.E.T.; Funding Acquisition, A.G. and R.E.T.

Declaration of interest

The authors declare no competing interests.

the IL-1β/IL-1RN axis and a gene set in the “receptor activity chemokine” cluster. Our results should facilitate AD therapeutics targeting these receptors.

In Brief

Microglial receptors, CD33 and TREM2, exhibit opposite effects on Aβ pathology and microglial activity in AD mice. In crosstalk between these receptors, TREM2 is required for differential gene expression in *5xFAD* mice deficient for *CD33*, and acts downstream of CD33.

Introduction

Alzheimer’s disease (AD) is the most common neurodegenerative disorder and the leading cause of dementia among the elderly (Tanzi, 2012). Genome-wide association studies have identified >30 genetic loci for AD, many related to immune response and microglia (Efthymiou and Goate, 2017). Among these are *CD33* (Bertram et al., 2008; Hollingworth et al., 2011; Naj et al., 2011) and *TREM2* (Guerreiro et al., 2013; Jonsson et al., 2013). While microglia can clear amyloid beta (Aβ), they can also release pro-inflammatory cytokines leading to neuroinflammation (Hansen et al., 2018; Hickman et al., 2008). A better understanding of the mechanisms that control microglial activation could advance therapies for AD.

CD33 encodes a sialic-acid binding immunoglobulin-like lectin (Siglec-3) expressed on the surface of myeloid progenitor cells, monocytes, and macrophages. CD33 has been implicated in cell adhesion processes, endocytosis, inhibition of cytokine release, immune cell growth (Crocker et al., 2007), and regulation of Tlr4 signaling (Ishida et al., 2014). We previously showed that CD33 exhibits increased expression in microglial cells in AD brain and that the protective allele of *CD33* SNP rs3865444, was associated with reductions in CD33 expression and insoluble Aβ42 levels in AD brain (Griciuc et al., 2013). We also showed CD33 inhibited microglial uptake and clearance of Aβ42, and that plaque burden was reduced in *APP/PS1;CD33*$^{-/-}$ mice.

In contrast, the risk allele of rs3865444 was associated with decreased Aβ42 uptake and increased expression of CD33 and TREM2 in monocytes (Bradshaw et al., 2013; Chan et al., 2015). The protective allele of *CD33* SNP rs12459419 was associated with skipping of *CD33* exon 2 (Malik et al., 2013). Exon 2 encodes the sialic acid-binding domain, required for CD33-mediated inhibition of Aβ uptake in microglia (Griciuc et al., 2013). Higher CD33 expression levels in the brain were associated with greater cognitive decline (Karch et al., 2012) and increased AD pathology (Walker et al., 2015). Collectively, these findings support CD33 as a therapeutic target in AD (Griciuc et al., 2013).

The AD risk factor *TREM2* is an immunoreceptor expressed on myeloid cells, primarily microglia, where it regulates inflammatory response (Tanzi, 2015; Yeh et al., 2017). TREM2 signals through the adaptor protein DAP12 (*TYROBP*) to suppress pro-inflammatory cytokine production (Turnbull et al., 2006), and promote phagocytosis (Takahashi et al., 2005) and biosynthetic metabolism (Ulland et al., 2017). Reported TREM2 ligands include anionic lipids (Wang et al., 2015), lipidated ApoE (Atagi et al., 2015; Bailey et al., 2015;

Yeh et al., 2016), and Aβ oligomers (Zhao et al., 2018; Zhong et al., 2018). AD-associated *TREM2* loss-of-function mutations reduced ligand-dependent activation of TREM2 signaling (Lessard et al., 2018; Song et al., 2017). Soluble TREM2 is elevated in AD cerebrospinal fluid (Suarez-Calvet et al., 2016).

TREM2 knock-out impaired microglial activation and clustering around Aβ plaques, and increased Aβ plaque load at late stages of disease (Jay et al., 2015; Ulrich et al., 2014; Wang et al., 2015). Moreover, *TREM2* knock-out disrupted the microglial barrier (Wang et al., 2016; Yuan et al., 2016). Conversely, *TREM2* overexpression in AD mouse models reduced plaque load and upregulated phagocytosis genes (Lee et al., 2018). The AD-linked R47H variant of *TREM2* impaired microgliosis in the *5xFAD* mouse model (Song et al., 2018).

Here, we investigated the crosstalk between CD33 and TREM2 in AD pathogenesis by generating single and double *CD33/TREM2* knock-out mice on wild-type (WT) and *5xFAD* backgrounds. *CD33* knock-out decreased Aβ pathology and improved cognition in *5xFAD* mice; both of which were abrogated by additional *TREM2* knock-out. *TREM2* knock-out reduced clustering of $Iba1^+$ myeloid cells around plaques, which could not be rescued by *CD33* knock-out. *CD33* and/or *TREM2* knock-out reprogrammed microglial gene expression signatures in *5xFAD* mice in an age-dependent manner. Differential gene expression in *5xFAD;CD33*$^{-/-}$ microglia depended on the presence of *TREM2*. These data suggest that TREM2 acts downstream of CD33, and that loss of microglial clearance capacity might be reversed by therapeutic inhibition of CD33 or activation of TREM2.

Results

CD33 knock-out restores cognitive function in *5xFAD* mice, which is abrogated by additional knock-out of *TREM2*

To test whether CD33 and TREM2 impact cognitive function in AD mice, we inactivated *CD33* and/or *TREM2* function in the *5xFAD* mouse (Oakley et al., 2006). WT, *CD33*$^{-/-}$, *TREM2*$^{-/-}$, *CD33*$^{-/-}$*;TREM2*$^{-/-}$, *5xFAD*, *5xFAD;CD33*$^{-/-}$, *5xFAD;TREM2*$^{-/-}$ and *5xFAD;CD33*$^{-/-}$*;TREM2*$^{-/-}$ mice were tested at 7 months of age for locomotor activity, anxiety levels and exploratory behavior in the open-field arena. We found no significant differences between the mouse groups for total distance travelled during exploration of the arena (Figure 1A) and total time spent in the center of the arena (Figure 1B).

To assess spatial learning and memory in 7-month-old mice, we employed the Morris water maze test (Vorhees and Williams, 2006) on the same mouse cohort. For training trials, a two-way repeated measures ANOVA revealed significant effects for days ($F_{(6,360)}=71.24$, $p<0.0001$) and for groups ($F_{(7,60)}=5.781$, $p<0.0001$), but not for interaction ($F_{(42,360)}=1.407$, $p=0.0539$, Figure 1C). *5xFAD;CD33*$^{-/-}$ mice displayed improved spatial learning versus *5xFAD;CD33*$^{-/-}$*;TREM2*$^{-/-}$ mice on days 6 and 7 (Figure 1C, $p<0.01$ and $p<0.05$, respectively, two-way ANOVA, Tukey's test). Training and test phases of platform locations are shown in Figure S1A.

On day 8, memory recall evaluation was conducted using the probe test (removed platform). We found no significant differences in latency to the target quadrant (Figure S1B) or time

spent in the target quadrant (Figure S1C). However, based on time spent in the area surrounding the missing platform (platform plus), we found significant differences (Figure 1D, Kruskal-Wallis ANOVA, $p<0.0001$). *5xFAD* mice showed impaired retention memory compared to WT (Figure 1D, $p<0.01$). Retention memory improved in *5xFAD;CD33*$^{-/-}$ mice compared to *5xFAD* ($p<0.05$), *5xFAD;TREM2*$^{-/-}$ ($p<0.05$) and *5xFAD;CD33*$^{-/-}$*;TREM2*$^{-/-}$ ($p<0.01$) mice (Figure 1D, Kruskal-Wallis ANOVA, Dunn's test).

Similarly, based on the number of platform plus crossovers, we found significant differences among the mouse groups (Figure 1E, one-way ANOVA, $F_{(7,60)}=9.134$, $p<0.0001$). *5xFAD* mice exhibited impaired retention memory compared to WT (Figure 1E, $p<0.01$). Retention memory improved in *5xFAD;CD33*$^{-/-}$ mice compared to *5xFAD* ($p<0.01$), *5xFAD;TREM2*$^{-/-}$ ($p<0.01$) and *5xFAD;CD33*$^{-/-}$*;TREM2*$^{-/-}$ ($p<0.01$) mice (Figure 1E, one-way ANOVA, Tukey's test). For all groups, no differences were observed in swim speed (Figure 1F) or latencies to the visible platform (Figure 1G). In summary, *CD33* knock-out significantly improved retention memory defects in *5xFAD* mice. These effects were abrogated by additional knock-out of *TREM2*, suggesting TREM2 functions downstream of CD33.

CD33 and TREM2 have opposite effects on amyloid beta in *5xFAD* mice; Knock-out of *TREM2* abrogates the effects of *CD33* knock-out on amyloid beta pathology

Next, we explored Aβ in tris-buffered saline (TBS)-soluble and formic acid (FA)-soluble fractions of cortex from 8-month-old *5xFAD*, *5xFAD;CD33*$^{-/-}$, *5xFAD;TREM2*$^{-/-}$ and *5xFAD;CD33*$^{-/-}$*;TREM2*$^{-/-}$ mice, by Aβ ELISA. Levels of TBS-soluble Aβ40 and Aβ42 were similar in all groups (Figures 2A and2B), whereas levels of FA-soluble Aβ40 and Aβ42 were markedly increased in *5xFAD;TREM2*$^{-/-}$ mice versus *5xFAD* (Figures 2C and2D). In contrast, levels of FA-soluble Aβ42 were decreased in *5xFAD;CD33*$^{-/-}$ versus *5xFAD*, *5xFAD;TREM2*$^{-/-}$ and *5xFAD;CD33*$^{-/-}$*;TREM2*$^{-/-}$ mice (Figure 2D). Knock-out of *TREM2* abrogated the reduction in Aβ in *5xFAD;CD33*$^{-/-}$ mice. Knock-out of *TREM2* did not impact levels of Aβ in *5xFAD* mice at 6 months of age (Figures S2A–S2D).

We next investigated whether *CD33* and *TREM2* knock-out impacts Aβ deposition. Coronal sections from 8-month-old mice were analyzed for amyloid plaque burden in cortex and hippocampus using the 3D6 antibody (Griciuc et al., 2013). 3D6 did not label control brains (Figure S2E). In comparison to *5xFAD,* Aβ plaque burden was robustly decreased in the cortex and hippocampus of *5xFAD;CD33*$^{-/-}$, and markedly increased in *5xFAD;TREM2*$^{-/-}$ mice (Figures 2E–2G). *5xFAD;CD33*$^{-/-}$ mice displayed dramatically reduced Aβ plaque burden in cortex and hippocampus compared to both *5xFAD;TREM2*$^{-/-}$ and *5xFAD;CD33*$^{-/-}$*;TREM2*$^{-/-}$ mice (Figures 2E–2G). *5xFAD;CD33*$^{-/-}$*;TREM2*$^{-/-}$ mice exhibited significantly increased cortical Aβ plaque load relative to *5xFAD* (Figure 2F), similar to that observed in *5xFAD;TREM2*$^{-/-}$ mice. *TREM2* knockout did not modulate Aβ plaque burden in younger (6-month-old) *5xFAD* mice (Figures S2F–S2H), indicating that *TREM2* knock-out increases amyloid plaque load at later stages of disease progression (e.g. 8 months of age). In summary, knock-out of *TREM2* abrogated the reduction in Aβ

pathology observed in *5xFAD;CD33*$^{-/-}$ mice, suggesting TREM2 functions downstream of CD33.

TREM2 knock-out leads to neurodegeneration in *5xFAD* mice, which is not rescued by additional knock-out of *CD33*

Next, we investigated the impact of *CD33* and *TREM2* knock-out on neuronal counts in 8-month-old *5xFAD* hippocampal CA1. WT, *CD33*$^{-/-}$, *TREM2*$^{-/-}$ and *CD33*$^{-/-}$*;TREM2*$^{-/-}$ mice displayed no differences in the number of NeuN^{+} (mature) neurons in CA1 (Figures 3A and3B). There was also no significant difference in neuronal cell numbers among WT, *5xFAD* and *5xFAD;CD33*$^{-/-}$ mice. The numbers of NeuN^{+} cells were significantly reduced in both *5xFAD;TREM2*$^{-/-}$ and *5xFAD;CD33*$^{-/-}$*;TREM2*$^{-/-}$ mice compared to *5xFAD* (Figures 3A and3B). These three lines showed no differences in spatial learning and retention memory (Morris water maze; Figures 1C–1E). This may be due to fast kinetics of Aβ deposition in *5xFAD* mice leading to a ceiling effect on cognitive deficits by 7 months of age. *5xFAD;CD33*$^{-/-}$ mice exhibited increased number of NeuN^{+} cells compared to *5xFAD;TREM2*$^{-/-}$ and *5xFAD;CD33*$^{-/-}$*;TREM2*$^{-/-}$ mice (Figure 3B). These results were confirmed using hematoxylin and eosin staining (Figures S3A and S3B). Collectively, our results show that knock-out of *TREM2* reduced CA1 pyramidal cell density in *5xFAD* mice, and could not be rescued by additional knock-out of *CD33*.

8-month-old mice WT, *CD33*$^{-/-}$, *TREM2*$^{-/-}$ and *CD33*$^{-/-}$*;TREM2*$^{-/-}$ mice exhibited no differences in the number of NeuN^{+} neurons in cortical layer 5 (Figures S3C and S3D). Numbers of cortical layer 5 NeuN^{+} cells were significantly reduced in *5xFAD* compared to WT mice. However, there were no significant differences among *5xFAD*, *5xFAD;TREM2*$^{-/-}$ and *5xFAD;CD33*$^{-/-}$*;TREM2*$^{-/-}$ mice. Numbers of cortical layer 5 NeuN^{+} cells were significantly increased in *5xFAD;CD33*$^{-/-}$ mice compared to *5xFAD*, *5xFAD;TREM2*$^{-/-}$ and *5xFAD;CD33*$^{-/-}$*;TREM2*$^{-/-}$ mice (Figures S3C and S3D). Thus, *CD33* knock-out increased pyramidal cell density in cortical layer 5 in *5xFAD* mice, and this was abrogated by additional knock-out of *TREM2*.

To investigate the effects of *CD33* and *TREM2* knock-out on neurodegeneration in 8-month-old *5xFAD* mice, we stained brain sections with an antibody specific for activated Caspase-3 and assessed cell loss. WT, *CD33*$^{-/-}$, *TREM2*$^{-/-}$ and *CD33*$^{-/-}$*;TREM2*$^{-/-}$ mice showed very few Caspase3^{+} cells in cortex and hippocampus (Figures 3D and3E). Conversely, *5xFAD* mice exhibited increased numbers of Caspase-3^{+} cells compared to WT. The numbers of Caspase-3^{+} cells were increased in cortex and hippocampus of both *5xFAD;TREM2*$^{-/-}$ and *5xFAD;CD33*$^{-/-}$*;TREM2*$^{-/-}$ mice versus *5xFAD* (Figures 3C–3E). In contrast, *5xFAD;CD33*$^{-/-}$ mice showed reduced numbers of Caspase-3^{+} cells in cortex and hippocampus versus *5xFAD*, *5xFAD;TREM2*$^{-/-}$ and *5xFAD;CD33*$^{-/-}$*;TREM2*$^{-/-}$ mice (Figures 3C–3E). Thus, CD33 and TREM2 have opposite effects on neurodegeneration in *5xFAD* mice. In conclusion, the attenuation in neurodegeneration observed in *5xFAD;CD33*$^{-/-}$ versus *5xFAD* mice, was abrogated by additional knock-out of *TREM2.*

Reduced Iba1$^+$ cell numbers and clustering of Iba1$^+$ cells around Aβ plaques in *5xFAD;TREM2$^{-/-}$* mice are not rescued by additional knock-out of *CD33*

Next, we investigated whether *CD33* and/or *TREM2* knock-out impact the response of Iba1$^+$ myeloid cells to Aβ deposition in 8-month-old *5xFAD* mice. Iba1$^+$ cells were evident around plaques (Figure 4A). Numbers of Iba1$^+$ cells were increased in *5xFAD* mice versus WT, and comparable in cortex and hippocampus of WT, *CD33$^{-/-}$*, *TREM2$^{-/-}$* and *CD33$^{-/-}$;TREM2$^{-/-}$* mice (Figures 4B, 4C and S4A). *5xFAD;TREM2$^{-/-}$* and *5xFAD;TREM2$^{-/-}$;CD33$^{-/-}$* mice displayed reduced numbers of Iba1$^+$ cells in cortex and hippocampus versus *5xFAD* (Figures 4A–4C).

We next quantified the number of Iba1$^+$ cells around plaques of similar sizes (Figures S4B and S4C). The degree of Iba1$^+$ cell clustering around plaques was significantly decreased in cortex and hippocampus of both *5xFAD;TREM2$^{-/-}$* and *5xFAD;CD33$^{-/-}$;TREM2$^{-/-}$* mice versus *5xFAD* (Figures 4D and4E). Iba1$^+$ cell clustering around hippocampal plaques was also decreased in *5xFAD;CD33$^{-/-}$;TREM2$^{-/-}$* mice versus *5xFAD;TREM2$^{-/-}$* (Figure 4E), suggesting that CD33 and TREM2 might synergize in controlling the number of Iba1$^+$ cells around Aβ deposits. In *5xFAD;CD33$^{-/-}$* mice, numbers of Iba1$^+$ cells (Figures 4B and4C) and clustering of Iba1$^+$ cells around plaques (Figures 4D and4E) were unchanged versus *5xFAD*, but increased versus *5xFAD;TREM2$^{-/-}$* and *5xFAD;CD33$^{-/-}$;TREM2$^{-/-}$* mice (Figures 4A–4E). Thus, additional knockout of *CD33* did not rescue the reduction in numbers of Iba1$^+$ cells or clustering of Iba1$^+$ cells around plaques in *5xFAD;TREM2$^{-/-}$* mice.

No differences were noted in Iba1$^+$ cell body area among controls, WT, *CD33$^{-/-}$*, *TREM2$^{-/-}$* and *CD33$^{-/-}$;TREM2$^{-/-}$* (Figures S4D and S4E). Reduced Iba1$^+$ cell body area (Figures S4F and S4G) and increased distance between Iba1$^+$ cells and associated plaques (Figures 4F and4G) were observed in cortex and hippocampus of *5xFAD;TREM2$^{-/-}$* and *5xFAD;CD33$^{-/-}$;TREM2$^{-/-}$* mice versus *5xFAD*. *5xFAD;CD33$^{-/-}$* mice exhibited significantly shorter distance between Iba1$^+$ cells and adjacent plaques (Figures 4F and4G) and increased Iba1$^+$ cell body area (Figures S4F and S4G) in cortex and hippocampus versus *5xFAD;TREM2$^{-/-}$* and *5xFAD;CD33$^{-/-}$;TREM2$^{-/-}$* mice but not versus *5xFAD*. Thus, *TREM2* knock-out in *5xFAD* mice leads to increased distance between Iba1$^+$ cells and plaques as well as reduced Iba1$^+$ cell body area; additional knock-out of *CD33* did not rescue these effects.

Based on Iba1 labeling of both microglia and monocytes infiltrating into the brain, we evaluated the extent of overlap between Iba1$^+$ and P2ry12$^+$ cells. P2ry12 is selectively expressed in microglia (Hickman et al., 2013). Numbers of P2ry12$^+$Iba1$^+$ cells were comparable in cortex (Figures 4H and4I) and hippocampus (Figures S4H and 4J) of 8-month-old *5xFAD*, *5xFAD;CD33$^{-/-}$*, *5xFAD;TREM2$^{-/-}$* and *5xFAD;CD33$^{-/-}$;TREM2$^{-/-}$* mice. However, numbers of P2ry12$^+$Iba1$^+$ cells normalized to Iba1$^+$ cells were significantly increased in cortex and hippocampus of *5xFAD;TREM2$^{-/-}$* mice versus *5xFAD* and *5xFAD;CD33$^{-/-}$* mice (Figures 4K and4L). The percentage of P2ry12$^+$Iba1$^+$/Iba1$^+$ cells was increased in cortex (Figure 4K) but not hippocampus (Figure 4L) of *5xFAD;CD33$^{-/-}$;TREM2$^{-/-}$* mice versus *5xFAD* and *5xFAD;CD33$^{-/-}$* mice. Thus, *TREM2* knock-out leads to an increase in P2ry12$^+$Iba1$^+$/Iba1$^+$ cells in *5xFAD* mice, suggesting they

are resident microglia. The reduction in Iba1^{+} cells around plaques in *5xFAD* mice deficient for *TREM2* may be due to a lower number of macrophages derived from infiltrating monocytes.

We next examined whether knock-out of *CD33* affected the number of TREM2^{+} cells surrounding Congo red^{+} plaques in *5xFAD* mice. Numbers of TREM2^{+} cells around Aβ plaques were markedly increased in cortex (Figures S4I and S4J) but not hippocampus (Figure S4K) of *5xFAD;CD33*$^{-/-}$ mice in comparison to *5xFAD*. Thus, *CD33* knock-out leads to increased numbers of TREM2^{+} cells surrounding Aβ plaques in the cortex of *5xFAD* mice.

Differential gene expression changes in *5xFAD* microglia during Alzheimer's disease progression

We next analyzed microglial transcriptomes in forebrains from 4 and 8-month-old WT and *5xFAD* mice using microglia that were isolated as previously described (Hickman et al., 2013). We generated microglial RNA samples and performed RNA-seq. Next, we compared the microglial transcriptomes of *5xFAD* and WT mice at 4 and 8 months of age. We used $\log_2$FC>1 (upregulated, FC=fold change, 2-fold), $\log_2$FC<−1 (downregulated, 2-fold) and false discovery rate (FDR)<0.05 as cutoffs for the differential gene expression analysis for the whole study.

The 40 most differentially expressed (DE) genes showed striking differences in *5xFAD* versus WT microglia at 4 months (Figure 5A) and 8 months of age (Figure 5C). The overall expression profile of *5xFAD* versus WT microglia revealed 486 DE genes at 4 months (Figure 5B) and 1794 DE genes at 8 months (Figure 5D and Table S1). Most DE genes were upregulated both at 4 and 8 months with 98.97% and 85.73% of genes upregulated, respectively (Figures 5B and5D). The top DE genes at 8 months were also enriched at 4 months, however to a lesser extent (Figure 5E), suggesting that gene expression changes in *5xFAD* microglia were progressive with aging. We observed a significant induction of phagocytic and lipid metabolism genes, e.g. *Axl*, *Cst7*, *Lpl*, and *Apoe*. Highly upregulated genes included *Baiap2l2* (vesicle formation), *Hpse* and *Lox* (extracellular matrix remodeling), *Dcstamp* and *Gpnmb* (phagocytic control), *Tmem163* (lysosomal uptake of Zn^{2+}), *Actr3b* (actin cytoskeleton), *Atp6v0d2* (lysosomal proton pump), *Mamdc2,* and *Ctse* (autophagic proteolysis) (Figures 5A, 5C, 5E and Table S1).

We next examined microglial pro- and anti-inflammatory activation genes (Hickman et al., 2013) in *5xFAD* versus WT mice. 8-month-old *5xFAD* microglia displayed a significant upregulation of anti-inflammatory genes such as *Igf1*, *Clec7a*, *Spp1*, *Il1rn*, and *Lgals3* (Figure 5F). Interestingly, pro-inflammatory genes, *Cxcl10*, *Cxcl9*, *Bcl2a1a* and *Tnf*, as well as inflammasome-associated genes, *Il12b*, *Il1b* and *Ptgs2,* were concomitantly upregulated (Figure 5F and Table S1).

We next assessed the microglial sensome (Hickman et al., 2013) in 8-month-old *5xFAD* mice compared to WT. Genes encoding proteins that sense bacterial and fungal ligands (*Clec7a*, *Cd74*, *Tlr2*, and *Cxcl16*) and apoptotic neurons and lipids (*Trem2* and its adaptor *Tyrobp*) were significantly upregulated in *5xFAD* microglia (Figure 5G). Genes that were

concomitantly downregulated encoded proteins involved in microglial homeostasis (*Cx3cr1*, *P2ry13*, *P2ry12*, and *Tmem119*), and sensing soluble cytokines (*Ifngr1* and *Ccr5*) and sialic acids (*Cd33*; Figure 5G and Table S1).

Next, we performed Ingenuity Pathway Analysis (IPA) to identify pathways changed in microglia. 4-month-old *5xFAD* microglia showed upregulation and activation of interferon signaling, role of pattern recognition receptors in sensing bacteria and viruses, and other pathways (Table S2). 8-month-old *5xFAD* microglia exhibited upregulated and activated pathways including nitric oxide (NO), TREM1, interferon, IL-8, Ephrin receptor, TGF-β and IL1 signaling (Table S1 and S2). Venn diagrams revealed 431 shared transcripts that were upregulated (99.07%) or downregulated (0.93%) at both time points (Figure 5H and Table S1). In summary, *5xFAD* microglia exhibit reduced expression of microglial homeostatic genes and progressive increases in the expression of genes related to lipid metabolism, phagocytic, and pro- and anti-inflammatory pathways.

Differential gene expression in *5xFAD;CD33*$^{-/-}$ microglia depends on *TREM2*, whereas differential gene expression in *5xFAD;TREM2*$^{-/-}$ microglia does not depend on *CD33*

We next analyzed the impact of *CD33* and/or *TREM2* knock-out on the transcriptome of microglia in 4-month-old *5xFAD* mice using RNA-seq profiling. First, we compared *5xFAD;CD33*$^{-/-}$ and *5xFAD* microglial transcriptomes and summarized the 40 strongest DE genes (Figure 6A). *CD33* knock-out led to significant upregulation of *Ftl2*, *Kcnj14*, *Kcna5*, *Zfp473*, *Serpina3n*, *Hif3a* and other genes in *5xFAD* microglia. Downregulated genes included *Klk8*, *Klrd1*, *Unc5a*, and *Treml1* (Figure 6A). *5xFAD;CD33*$^{-/-}$ microglia yielded 299 enriched genes in comparison to *5xFAD* (275 upregulated; 24 downregulated; Figure 6B and Table S3). While IL-6, p38 MAPK, sphingosine-1-phosphate, NF-κB and acute phase response signaling pathways were upregulated and activated, the PPAR signaling pathway was inhibited in *5xFAD;CD33*$^{-/-}$ microglia (Tables S2 and S3). In sharp contrast, *CD33* knock-out resulted in only 10 DE genes when *TREM2* was also knocked out in *5xFAD* mice (Figures 6A and6B). 8 DE genes overlapped between the *5xFAD;CD33*$^{-/-}$*;TREM2*$^{-/-}$ versus *5xFAD;TREM2*$^{-/-}$ (10 DE genes in total) and *5xFAD;CD33*$^{-/-}$ versus *5xFAD* (299 DE genes in total) datasets (Figure S5A and Table S3). Thus, differential gene expression in *5xFAD;CD33*$^{-/-}$ microglia is contingent upon the presence of *TREM2*, suggesting TREM2 acts downstream of CD33 in regulating transcription in *5xFAD* microglia.

RNA-seq profiling in 4-month-old *5xFAD;TREM2*$^{-/-}$ microglia revealed 134 DE genes versus *5xFAD* (125 downregulated; 9 upregulated; Figures 6C, 6D and Table S3). Highly enriched transcripts revealed downregulation of phagocytic and lipid metabolism genes, e.g. *Axl*, *Cst7* and *Lpl*, as well as *Dcstamp*, *Tmem163, Lox*, *Actr3b*, *Atp6v0d2*, *Itgax*, *Il12b*, *Ctse*, *Fgf2* and *Mamdc2* (Figure 6C). Upregulated genes included *Treml4* (positive regulator of Tlr7 signaling), *Unc5cl*, and *Apobec2* (Figure 6C). Furthermore, *TREM2* knock-out in *5xFAD* microglia resulted in downregulation of pathways such as LXR/RXR activation, LPS/IL-1 mediated inhibition of RXR function and clathrin-mediated endocytosis signaling (Tables S2 and S3).

TREM2 knock-out led to 268 DE genes when *CD33* was also knocked out in *5xFAD* mice (238 downregulated; 30 upregulated; Figures 6C, 6D and Table S3). The strongest 40 DE

genes included *Atp6v0d2*, *Tmem163*, *Kcnk9*, *Dcstamp*, *Cst7*, *Axl*, *Lox*, *Actr3b*, and *Itgax* (Figure 6C) that were downregulated in 4-month-old *5xFAD;CD33*$^{-/-}$*;TREM2*$^{-/-}$ microglia versus *5xFAD;CD33*$^{-/-}$. Upregulated genes included *Treml4*, *Treml1*, *Unc5cl*, and *Apobec2* (Figure 6C). Pathways downregulated and inhibited in *5xFAD;CD33*$^{-/-}$*;TREM2*$^{-/-}$ microglia versus *5xFAD;CD33*$^{-/-}$ included activation of IRF by cytosolic pattern recognition receptors, TREM1 and IL-6 signaling (Tables S2 and S3). 117 genes overlapped in *5xFAD;TREM2*$^{-/-}$ versus *5xFAD* (134 DE genes in total) and *5xFAD;CD33*$^{-/-}$*;TREM2*$^{-/-}$ versus *5xFAD;CD33*$^{-/-}$ (268 DE genes in total) datasets (Figure S5A and Table S3). Therefore, *TREM2* knock-out impacts the differential expression of these 117 genes independently of *CD33*. *TREM2* knock-out resulted in 151 genes that were exclusively enriched when *CD33* was also knocked out in *5xFAD* microglia (Figure S5A and Table S3). Thus, differential gene expression owing to *TREM2* knock-out in *5xFAD* microglia was amplified by additional knock-out of *CD33*.

We proceeded to investigate the relationship of DE genes in the *5xFAD* versus WT dataset as a function of the presence or absence of CD33 and/or TREM2. For this purpose, we took the top 60 DE genes (p-value<0.001 and FDR<0.05) in *5xFAD* versus WT and hierarchically clustered the $\log_2$FC values across the *5xFAD;CD33*$^{-/-}$ versus *5xFAD,* *5xFAD;CD33*$^{-/-}$*;TREM2*$^{-/-}$ versus *5xFAD;TREM2*$^{-/-}$, *5xFAD;TREM2*$^{-/-}$ versus *5xFAD*, and *5xFAD;CD33*$^{-/-}$*;TREM2*$^{-/-}$ versus *5xFAD;CD33*$^{-/-}$ datasets (Figure 6E).

We identified three major clusters in the heatmap. Most genes in cluster 1 (*Baiap2l2* to *Axl*, 18 genes) were dependent on TREM2, but not CD33, and were extremely highly downregulated by *TREM2* knock-out (Figure 6E). These genes were related to vesicle formation and phagocytic activity (e.g. *Baiap2l2*, *Actr3b*, *Clec7a*, and *Axl*), autophagy (e.g. *Ctse*), lipid metabolism (e.g. *Cst7* and *Lpl*), growth factors (e.g. *Igf1*), as well as others. Most genes in cluster 2 (*Apoe* to *Cdk18*, 26 genes) were dependent on TREM2, but not CD33 (e.g. *Lgals3*, *Lyz2*, *Ifit2*, *Cd72*, *Il3ra*, *Cd52*, and *Ccl6*), and were moderately downregulated by *TREM2* knock-out. Most genes in cluster 3 (*Ch25h* to *Ank*, 16 genes), such as *Fgr*, *Xylt1*, *Atp1a3* and *Ldlr*, were dependent on TREM2, but not CD33, and were highly downregulated by *TREM2* knock-out.

Although *Hpse*, *Gpnmb* and *Lox* (cluster 1) and *Il1b* (cluster 3) were upregulated in *5xFAD;CD33*$^{-/-}$ versus *5xFAD,* this effect was abrogated in the *5xFAD;CD33*$^{-/-}$*;TREM2*$^{-/-}$ versus *5xFAD;TREM2*$^{-/-}$ dataset (Figure 6E), indicating that these genes were dependent on both CD33 and TREM2. In summary, most genes in cluster 1 (strongest), cluster 3 (second strongest) and cluster 2 (relatively weak) were dependent on TREM2, but not CD33, while a small set of genes was dependent on both CD33 and TREM2.

Next, we examined *Cd33*, *Trem2* and *Tyrobp* expression levels in all the datasets by RNAseq. We found no significant changes in expression levels of *Trem2* or *Tyrobp* in *CD33*$^{-/-}$ versus WT (Figure S5B) and *5xFAD;CD33*$^{-/-}$ versus *5xFAD* (Figure S5C) datasets at 4 and 8 months. Conversely, *Cd33* and *Tyrobp* expression levels did not change in *TREM2*$^{-/-}$ versus WT microglia (Figure S5D). While there was no change in *Cd33* expression levels at 4 months, there was a slight increase at 8 months in *5xFAD;TREM2*$^{-/-}$

versus *5xFAD* microglia (Figure S5E). Finally, we found a moderate decrease in *Tyrobp* levels at 4 and 8 months in *5xFAD;TREM2*$^{-/-}$ versus *5xFAD* microglia (Figure S5E). Thus, *CD33* and *TREM2* knock-out did not significantly impact each other's expression levels in *5xFAD* mice, while *TREM2* knock-out had a small effect on *Tyrobp* expression.

We next investigated the effects of *CD33* and *TREM2* knock-out on microglial activation and inflammasome genes in 4-month-old *5xFAD* mice. For *5xFAD* versus WT microglia, we observed concurrent upregulation of anti-inflammatory genes including *Igf1*, *Clec7a* and *Il1rn*, pro-inflammatory genes, *Cxcl9*, *Cxcl10* and *Tnf*, and inflammasome-associated genes, *Il12b*, *Il1b* and *Ptgs2* (Figure S6A and Table S4). Levels of anti-inflammatory genes, *Cxcl1*, *Il1rn* and *Car2*, and inflammasome genes, *Il1b*, *Il33* and *Ptgs2*, were significantly increased in *5xFAD;CD33*$^{-/-}$ microglia compared to *5xFAD* (Figure S6B). In contrast, *TREM2* knock-out led to concurrent downregulation of anti-inflammatory (e.g. *Clec7a*, *Igf1* and *Gas7*), pro-inflammatory (e.g. *Cxcl10 and Bcl2a1a*) and inflammasome genes (e.g. *Il12b*, *Il1b* and *Ptgs2*) in *5xFAD* microglia (Figure S6C).

Expression of anti-inflammatory, pro-inflammatory and inflammasome genes were markedly decreased in *5xFAD;CD33*$^{-/-}$*;TREM2*$^{-/-}$ microglia relative to both *5xFAD* and *5xFAD;CD33*$^{-/-}$ (Figures S6D, S6E and Table S4). The expression profiles of inflammation genes were similar between *5xFAD;TREM2*$^{-/-}$ and *5xFAD;CD33*$^{-/-}$*;TREM2*$^{-/-}$ mice, but not *5xFAD;CD33*$^{-/-}$ (versus *5xFAD*). Thus, additional knock-out of *CD33* did not reverse the downregulation of microglial activation and inflammasome genes in *5xFAD;TREM2*$^{-/-}$ mice.

Crosstalk between CD33 and TREM2 in *5xFAD* microglia includes regulation of the IL-1β/IL-1RN axis and a gene set related to the receptor activity chemokine cluster

Next, we assessed the effects of aging on *CD33* and *TREM2*-mediated regulation of gene expression in *5xFAD* mice. For this purpose, we isolated microglia from 8-month-old *5xFAD*, *5xFAD;CD33*$^{-/-}$ and *5xFAD;TREM2*$^{-/-}$ mice, and conducted RNA-seq. The strongest 40 DE genes (Figure 7A) in 8-month-old *5xFAD;CD33*$^{-/-}$ microglia were also DE genes in 4-month-old *5xFAD;CD33*$^{-/-}$ (versus *5xFAD*). Highly enriched genes, e.g. *Ftl2*, *Kcnj14*, *Slc6a16*, and *Zfp473* were upregulated in *5xFAD;CD33*$^{-/-}$ mice throughout aging. Other genes, e.g. *Serpina3n* and *Cxcl13,* were highly upregulated at 8 months in *5xFAD;CD33*$^{-/-}$ microglia but to a lesser degree at 4 months (Figure 7A). The expression profile of 8-month-old *5xFAD;CD33*$^{-/-}$ microglia (versus *5xFAD*) revealed 282 DE genes (274 upregulated; 8 downregulated; Figure 7C and Table S5). *CD33* knock-out in *5xFAD* mice resulted in upregulation and activation of pathways that included leukocyte extravasation, acute phase response, phospholipase C and IL-8 signaling at 8 months (Tables S2 and S5).

Figure 7B shows the strongest 40 DE genes in 8-month-old *5xFAD;TREM2*$^{-/-}$ microglia that were also DE genes at 4 months (versus *5xFAD*). Downregulated genes included *Dcstamp*, *Tmem163*, *Atp6v0d2, Gpnmb*, *Mamdc2*, *Spp1*, and *Lpl* (Figure 7B). While some genes, e.g. *Treml4*, *Unc5cl* and *Cd5l*, were consistently upregulated during aging, others were upregulated later in age, e.g. *Ms4a4d* and *Serpina3g* (Figure 7B). *5xFAD;TREM2*$^{-/-}$ microglia versus *5xFAD* revealed 214 DE genes at 8 months (186 downregulated; 28

upregulated; Figure 7D and Table S5). Pathways downregulated and inhibited in 8-month-old *5xFAD;TREM2*$^{-/-}$ mice (versus *5xFAD*) included Toll-like receptor signaling, Th1 pathway, TREM1, IL-6, IL-8 and acute phase response signaling (Tables S2 and S5).

96 DE genes in *5xFAD;CD33*$^{-/-}$ microglia (versus *5xFAD*) overlapped in 4 and 8-month-old mice (92 upregulated; 4 downregulated; Figure S7A and Table S6). 183 genes were upregulated in 4month-old, but not 8-month-old *5xFAD;CD33*$^{-/-}$ mice (versus *5xFAD*) and were related to IL-6, IL-10 and PPAR signaling, phagosome formation, and NRF2-mediated oxidative stress response pathways. 182 genes were upregulated in 8-month-old, but not 4-month-old *5xFAD;CD33*$^{-/-}$ mice (versus *5xFAD*) and were associated with pathways including CCR5 signaling, protein kinase A, IL-8, acute phase response, and P2Y purinergic receptor signaling (Figure S7A and Table S6).

Conversely, *TREM2* knock-out resulted mainly in downregulation of gene expression in *5xFAD* microglia. 4 and 8-month-old *5xFAD;TREM2*$^{-/-}$ mice (versus *5xFAD*) shared 96 downregulated and only 6 upregulated transcripts (Figure S7A and Table S6). The 96 genes belonged to pathways that included clathrin-mediated endocytosis, phagosome maturation, and TREM1, IL-6 and IL-8 signaling. 90 genes were downregulated in 8-month-old (but not 4-month-old) *5xFAD;TREM2*$^{-/-}$ microglia (versus *5xFAD*). These genes were related to pathways including antigen presentation, Th1 pathway, and production of NO and reactive oxygen species (Figure S7A and Table S6). Collectively, our data show that DE genes related to IL-6, IL-8 and acute phase response signaling, as well as phagosome formation and maturation in *5xFAD;CD33*$^{-/-}$ and *5xFAD;TREM2*$^{-/-}$ mice were upregulated and downregulated, respectively.

While 299, 134 and 209 DE genes were found in 4-month-old *5xFAD;CD33*$^{-/-}$, *5xFAD;TREM2*$^{-/-}$ and *5xFAD;CD33*$^{-/-}$*;TREM2*$^{-/-}$ microglia relative to *5xFAD*, respectively, we found only 9, 22, and 23 DE genes in *CD33*$^{-/-}$, *TREM2*$^{-/-}$ and *CD33*$^{-/-}$*;TREM2*$^{-/-}$ compared to WT, respectively (Figure S7B and Table S6). Similar DE patterns were observed at 8 months of age (Figure S7C and Table S6). Thus, knock-out of *CD33* and/or *TREM2* resulted in greater differential gene expression in the presence of AD pathology in *5xFAD* mice versus WT.

Knock-out of *CD33* and *TREM2* conferred opposite regulatory effects on six genes *Il1b*, *Il1rn*, *Gpnmb*, *Lox*, *Vegfa*, and *Mamdc2*, at 4 months, and two genes, *Ftl2* and *Cxcl13*, at 8 months in *5xFAD* mice (upregulated in *5xFAD;CD33*$^{-/-}$ microglia; downregulated in *5xFAD;TREM2*$^{-/-}$ microglia (versus *5xFAD*); Figures S8A and S8B).

We used STRING protein-protein analyses to identify significant networks among upregulated genes from *5xFAD;CD33*$^{-/-}$ and downregulated genes from *5xFAD;TREM2*$^{-/-}$ microglia (versus *5xFAD*) at 4 and 8 months. 16 proteins overlapped across both ages, with IL-1β and IL-1RN at the center of inflammation pathways in *5xFAD;CD33*$^{-/-}$ and *5xFAD;TREM2*$^{-/-}$ microglia (Figures S8A and S8B). IL-1RN is structurally similar to IL-1β, but functions as an antagonist that binds to IL-1 receptor type 1. Knock-out of *CD33* resulted in concurrent upregulation of IL-1β, IL1RN and other cytokines, which regulate

microglial activation. Conversely, *TREM2* knock-out led to decreased expression levels of IL-1β, IL-1RN and other cytokines.

We further validated our RNAseq data by qPCR using microglia that were isolated from 4-month-old *5xFAD*, *5xFAD;CD33*$^{-/-}$ and *5xFAD;TREM2*$^{-/-}$ mice. We performed qPCR analysis on four transcripts, including *Il1b*, *Il1rn*, *Gpnmb*, and *Vegfa*. As seen in our RNAseq analysis, these transcripts were upregulated in *5xFAD;CD33*$^{-/-}$ and downregulated in *5xFAD;TREM2*$^{-/-}$ microglia versus *5xFAD* (Figure S8A and Table S3). The qPCR analysis also showed that *Il1b*, *Il1rn*, *Gpnmb*, and *Vegfa* were significantly upregulated in *5xFAD;CD33*$^{-/-}$ and downregulated in *5xFAD;TREM2*$^{-/-}$ microglia compared to *5xFAD* (Figures S8C–S8F). The results obtained from qPCR and RNAseq were highly comparable, suggesting that our RNAseq data are supported by qPCR data.

To explore potential biological mechanisms, we performed a gene set enrichment analysis on the *5xFAD;CD33*$^{-/-}$ and *5xFAD;TREM2*$^{-/-}$ (versus *5xFAD*) datasets at 8 months, using a gene set containing all three divisions of gene ontology: biological process, molecular function, and cellular component (Merico et al., 2010). Using a p-value<0.001 and FDR<0.05, we found 277 gene sets enriched for *5xFAD;CD33*$^{-/-}$ versus *5xFAD* and 342 gene sets for *5xFAD;TREM2*$^{-/-}$ versus *5xFAD* dataset. The top 30 significant gene sets are shown in Figure 7E. The gene set related to IL-8 and CXCR2-mediated signaling events showed significant enrichment in the *5xFAD;CD33*$^{-/-}$ versus *5xFAD* group.

We then generated, clustered and annotated enrichment maps for both datasets using Cytoscape software (Figure 7F). The *5xFAD;CD33*$^{-/-}$ versus *5xFAD* enrichment map revealed clusters including morphogenesis branching development, extracellular collagen matrix, ERK1 tyrosine kinase and others. The *5xFAD;TREM2*$^{-/-}$ versus *5xFAD* enrichment map showed clusters such as IL-4/12, cytokine production secretion, receptor activity chemokine and others. We found four edges (connections) of varying sizes of gene set overlap between the extracellular collagen matrix (in the *5xFAD;CD33*$^{-/-}$ group) and chemokine receptor activity cluster (in the *5xFAD;TREM2*$^{-/-}$ group, Figure 7F).

In summary, neuroinflammation in *5xFAD* mice is influenced by the crosstalk between CD33 and TREM2, which includes regulation of the IL-1β/IL-1RN axis and gene sets related to the extracellular collagen matrix and receptor activity chemokine clusters.

Discussion

We carried out comprehensive analysis of the crosstalk between CD33 and TREM2 in a mouse model of AD. *CD33* knock-out resulted in improved cognition and decreased Aβ pathology in *5xFAD* mice; these effects were abrogated by additional knock-out of *TREM2*. Conversely, *TREM2* knock-out reduced Iba1^{+} cell numbers, increased Aβ pathology, and exacerbated neurodegeneration in *5xFAD* mice. Since these effects could not be rescued by additional knock-out of *CD33*, TREM2 acts downstream of CD33 in modulating microglial pathology in AD.

CD33 was also reported to negatively regulate Tlr4 signaling (Ishida et al., 2014); C1q binding to CD33 led to activation of CD33/LAIR-1 inhibitory motifs (Son et al., 2017).

TREM2 expression was increased by *CD33* AD risk allele rs3865444^{C} and decreased by CD33 immunosuppression in human monocytes (Chan et al., 2015). *CD33* knock-out did not modulate *Trem2* expression levels but increased the numbers of TREM2^{+} cells surrounding Aβ plaques in the cortex of *5xFAD* mice, suggesting CD33 might impact the expression pattern of TREM2.

Previous studies reported *TREM2* knock-out decreased (Jay et al., 2015; Krasemann et al., 2017) or did not impact (Wang et al., 2016) Aβ plaque burden during early disease. However, *TREM2* knock-out significantly increased Aβ plaque burden at late disease stages (Jay et al., 2017; Wang et al., 2015). We showed that TREM2 affects Aβ plaque load downstream of CD33. Moreover, *TREM2* knock-out reduced pyramidal cell density in CA1 and exacerbated neurodegeneration in *5xFAD* cortex and hippocampus. While *CD33* knock-out increased pyramidal cell density in cortical layer 5 and attenuated neurodegeneration in cortex and hippocampus of *5xFAD* mice, these effects were abrogated by additional knock-out of *TREM2*. Thus, TREM2 functions downstream of CD33 in regulating neuronal cell loss in *5xFAD* mice.

In agreement with previous studies, *TREM2* knock-out decreased clustering of Iba1^{+} cells around plaques (Jay et al., 2015; Ulrich et al., 2014; Wang et al., 2015). We showed TREM2 acts downstream of CD33 in regulating Iba1^{+} cell response in *5xFAD* mice. In a tauopathy mouse model, *TREM2* knock-out reduced pro-inflammatory microglial activation, but ameliorated neurodegeneration (Leyns et al., 2017).

We showed *TREM2* knock-out leads to an increase in P2ry12^{+}Iba1^{+}/Iba1^{+} cells in *5xFAD* mice, suggesting they are resident microglia. These results demonstrate a reduction in Aβ plaque-associated macrophages, but not parenchymal microglia in *TREM2*-deficient *5xFAD* mice in agreement with (Jay et al., 2015). TREM2 has been previously reported to bind both Aβ oligomers and ApoE (Atagi et al., 2015; Yeh et al., 2017; Yeh et al., 2016), known to regulate Aβ deposition.

Overexpression of human *TREM2* reduced Aβ plaque load and improved memory performance in AD mice (Lee et al., 2018). Overexpression of human *TREM2*-R47H in *5xFAD* mice lacking endogenous *TREM2* impaired microgliosis and reduced microglial activation, but, neither mutant, nor WT *TREM2* affected plaque burden (Song et al., 2018). This discrepancy may be due to the presence of both human and mouse TREM2 in Lee et al.

RNA-seq profiling of microglia in *5xFAD* versus WT mice revealed downregulation of microglial homeostatic genes as well as progressive increases in both pro- and anti-inflammatory pathway genes. *CD33* knock-out upregulated genes related to phagocytosis, microglial activation and cytokine production in *5xFAD* mice, whereas *TREM2* knock-out downregulated these genes. *TREM2* knock-out was previously reported to downregulate pro-inflammatory cytokines (Jay et al., 2015; Wang et al., 2015), whereas overexpression of human *TREM2* upregulated microglial phagocytosis genes (Lee et al., 2018).

We also showed that TREM2 acted downstream of CD33 based on expression profiling. Recently, TREM2 has been shown to sustain microglial metabolism and survival (Ulland et al., 2017). It is possible that knock-out of *CD33* cannot activate microglia if *TREM2* is also

knocked out, because microglia are metabolically impaired and fail to survive. While CD33 and TREM2 are cell surface receptors binding different ligands, both functionally interact with DAP12/TYROBP, either directly (TREM2) or via common intracellular signaling factors (CD33). Thus, DAP12 and interacting signaling molecules, e.g. SHP1/2, Syk, and PI3K, are likely key effectors of crosstalk between CD33 and TREM2.

Recently, a unique population of AD-associated microglia has been characterized by TREM2-dependent upregulation of phagocytic and lipid metabolism genes (Keren-Shaul et al., 2017). Here, *TREM2* knock-out dramatically downregulated phagocytic and lipid metabolism genes in *5xFAD* microglia. However, another study suggested that the TREM2-APOE pathway mediated a switch from the homeostatic to neurodegenerative microglia phenotype in *APP-PS1* mice (Krasemann et al., 2017). These contradictory findings might be explained by distinct roles of TREM2 at different stages of AD pathology (Jay et al., 2017).

Our RNAseq analyses provided candidates that may underlie the changes in microglial response in *5xFAD* mice in which *CD33* and/or *TREM2* were knocked out. *Il1b*, *Gpnmb*, *Cst7*, *Atp6v0d2*, and *Spp1* were downregulated in *5xFAD;TREM2*$^{-/-}$ versus *5xFAD* mice. Interestingly, *Il1b*, *Gpnmb*, *Cst7*, *Atp6v0d2*, and *Spp1* were upregulated in *5xFAD* mice overexpressing human *TREM2* (Lee et al., 2018; Song et al., 2018). These genes may represent transcriptional targets of TREM2-dependent signaling in the context of AD.

In *5xFAD* mice, *CD33* knock-out upregulated, while *TREM2* knock-out downregulated *Il1b*, *Il1rn*, *Gpnmb*, *Lox*, *Vegfa*, and *Mamdc2*. The IL-1β/IL-1RN axis was central in overlapping inflammation pathways in *5xFAD;CD33*$^{-/-}$ and *5xFAD;TREM2*$^{-/-}$ microglia. Thus, knock-out of *CD33* and *TREM2* confer opposite regulatory effects on the agonist and antagonist of the IL-1 receptor type 1 (IL-1β and IL-1RN, respectively). Pro-inflammatory cytokines, e.g. IL-1β, impair microglial phagocytosis (Hickman et al., 2008). Interestingly, transplantation of neural precursor cells overexpressing IL-1RN or IL-1RN injection rescued spatial memory impairment in AD mice (Ben-Menachem-Zidon et al., 2014). *Gpnmb* controls trafficking of cellular debris for degradation in macrophages (Li et al., 2010). Finally, treatment with VEGFA improved behavioral deficits and decreased Aβ deposits in *APP/PS1* mice (Herran et al., 2013).

VEGF and IL-1β levels were elevated in plasma of amyotrophic lateral sclerosis (ALS) patients (Hu et al., 2017). *IL1B* mRNA levels were also increased in peripheral blood monocytes of multiple sclerosis (MS) patients (Heidary et al., 2014), while IL-1RN levels were diminished in serum and cerebrospinal fluid of MS patients (Fernandez-Paredes et al., 2017). GPNMB expression was higher in the serum of ALS patients versus controls (Tanaka et al., 2012). Finally, GPNMB expression was also increased around MS lesions (Hendrickx et al., 2017).

In summary, we show for the first time that TREM2 acts downstream of CD33 in modulating cognition, amyloid pathology, neurodegeneration, microgliosis and microglial gene expression in *5xFAD* mice. Inhibiting CD33 and/or increasing TREM2 activity represent potential therapies for AD, e.g. by gene therapy, small molecules, or

immunotherapy. Collectively, these data should greatly facilitate novel therapeutic approaches for the prevention and treatment of AD based on modulation of microglial activation state.

STAR * METHODS

CONTACT FOR REAGENT AND RESOURCE SHARING

Further information and request for reagents should be directed to and will be fulfilled by the Lead Contact Rudolph E. Tanzi (tanzi@helix.mgh.harvard.edu).

EXPERIMENTAL MODEL AND SUBJECT DETAILS

Animal breeding and husbandry—*5xFAD* mice (Oakley et al., 2006) were purchased from the Jackson Laboratory (MMRRC) and backcrossed onto the C57BL/6J background for seven generations before breeding with other mouse strains. Constitutive *CD33* knock-out mice were obtained from the Jackson Laboratory. Constitutive *TREM2* knock-out mice were generated at Washington University School of Medicine and were previously described (Turnbull et al., 2006). Both *CD33* and *TREM2* knock-out mouse strains are on the C57BL/6J background. *5xFAD* mice were crossed to $CD33^{-/-}$ and $TREM2^{-/-}$ mice in the C57BL/6J background. $CD33^{-/-}$ and $TREM2^{-/-}$ mice breed normally (Griciuc et al., 2013; Turnbull et al., 2006). The *5xFAD* mice lacking *CD33* and/or *TREM2* exhibited no gross anatomical defects. Matched numbers of mice of both sex (males and females) were used in the study. The age, number and sex of mice used for individual experiments are indicated in the figure legends. All mice were housed under standard conditions with free access to food and water. All animal experiments were performed in strict accordance with National Institutes of Health and approved by the Institutional Animal Care and Use Committee at Massachusetts General Hospital.

METHOD DETAILS

Behavioral tests—All the behavioral tests were conducted in the Animal Behavior Facility at Massachusetts General Hospital. For the open field exploration test, mice were placed in the center of the dimly lit chamber of the open field arena. Mouse movements were recorded and tracked by the automatic video tracking system EthoVision XT (Noldus) for 15 minutes. The area of the arena was virtually divided into a center zone (Pasquarella et al.) and four corner squares. Total distance traveled, the time spent in each area, and horizontal and vertical activity were monitored.

The Morris water maze test was performed with minor adjustment as previously described (Vorhees and Williams, 2006). Spatial memory testing was conducted in a circular tank (diameter 1.22 m) filled with opacified water at 23°C. The water tank was dimly lit and surrounded by a white curtain. The maze was virtually divided into four quadrants, with one containing a hidden platform (diameter 10 cm) that was submerged 0.5 cm below the water level. Four prominent cues were placed outside the maze as spatial references. Mice were placed in the water facing the tank wall at different start positions across trials in a quasi-random fashion to prevent strategy learning. Mice were allowed to search for the platform for 1 minute; if the mice did not find the platform, they were guided towards it where they

remained for 20 seconds. Each mouse went through four trials (one from each start position) per day for seven consecutive days. After each trial, the mouse was dried and placed back into its cage until the start of the next trial. All mouse movements were recorded by the computerized tracking system EthoVision XT (Noldus) that calculated distances moved and time required to reach the platform (escape latency), along with swim speed. The spatial probe trial was conducted 24 hours after the last training session (on day 8). For the probe trial, the platform was removed and mice were allowed to swim for 1 minute. The time spent by the mice in the area surrounding the location where the platform used to be (platform plus) was recorded. The platform plus surrounding the target is larger than the target itself, but smaller than the target quadrant. Data was calculated as time in the platform plus/60 sec*100% and is given in percentage. The number of times the mice crossed the platform plus is also shown. On days 9 and 10, the visual cued testing was conducted, where the platform was flagged and placed above the water surface. Mice were allowed to swim to the visible platform for 1 minute and each mouse performed two trials per day. Time required to reach the visible platform is shown.

Tissue collection and sample preparation—Mice were deeply anesthetized with CO_2 and transcardially perfused with 0.9% sodium chloride. The brains were quickly removed from the skull. The right brain hemisphere was submerged in ice-cold 0.9% sodium chloride. Cortex and hippocampus were dissected and snap frozen in dry ice. Samples were stored at −80°C until further processing. The left hemisphere was fixed in 4% paraformaldehyde for 72 hours at 4°C. Subsequently, the left hemisphere was dehydrated with ethanol and embedded in paraffin. Paraffin-embedded tissue was cut into 6 μm-thick coronal sections using a paraffin microtome, transferred onto microscope slides and stored at room temperature.

Aβ ELISA

Mouse cortices were homogenized in 5 volumes of tissue homogenization buffer [25 mM Tris-HCl at pH 7.4, 130 mM NaCl, 2.7 mM KCl, 5 mM EDTA, phosphatase inhibitor (Thermo Fisher Scientific), EDTA-free protease inhibitor cocktail (Roche) and 2 mM 1,10-phenantroline (Sigma Aldrich)], using a Polytron benchtop lab homogenizer (Wheaton) at 4°C. The homogenates were centrifuged at 100,000 *g* for 1 hour at 4°C using an Optima TL ultracentrifuge and a TLA 120.2 rotor (Beckman Coulter). Supernatants were collected and used to measure TBS-soluble Aβ. The pellet was extracted in 70% formic acid (equal volume of TBS) with a hand homogenizer (Wheaton) on ice. Samples were centrifuged at 100,000 *g* for 1 hour at 4°C and supernatants were collected. Formic acid supernatants were neutralized with 1M Tris-base, pH 11 (1:17 v:v) and samples were used to measure formic acid-soluble Aβ. TBS-soluble and formic acid-soluble Aβ were measured by sandwich ELISA using commercially available kits (Wako). The capture antibody was mouse monoclonal anti-human Aβ antibody (clone BNT77). HRP-conjugated monoclonal anti-human Aβ40 (clone BA27) and monoclonal anti-human Aβ42 (clone BC05) antibodies were used for detection of Aβ40 and Aβ42, respectively.

Immunohistochemistry and image analysis—Coronal sections were deparaffinized and incubated with 3% H_2O_2 to quench endogenous peroxidases for DAB staining. Antigen

retrieval was performed using Diva Decloaker (Biocare Medical) or citrate buffer (0.01M, pH 6.0, 0.05% Tween-20) in a microwave oven (95°C, 20 minutes). For immunostaining with the anti-Aβ antibody (clone 3D6 directed against Aβ residues 1–5), sections were incubated in 90% formic acid (Sigma Aldrich) for 5 minutes, after antigen retrieval. Sections were subsequently blocked using 2% BSA, 0.1% Triton X-100 in PBS, or alternatively with Antibody diluent (Cell Signaling). The following primary antibodies were added overnight at 4°C: anti-Aβ (mouse monoclonal, clone 3D6, 1:2500, Elan Pharmaceuticals), anti-cleaved Caspase-3 (rabbit monoclonal, 1:500, Cell Signaling), anti-Iba1 (rabbit polyclonal, 1:500, Wako), anti-Iba1 (goat polyclonal, 1:1000, Novus Biologicals), anti-P2ry12 (rabbit polyclonal, 1:2000, AnaSpec), and anti-TREM2 (sheep polyclonal, 1:50, R&D Systems). The primary antibody targeting NeuN (mouse monoclonal, 1:300, Millipore Sigma) was added for 1 hour at room temperature. Primary antibodies were detected using appropriate biotinylated secondary antibodies (1:300) and VECTASTAIN Elite ABC HRP kits (Vector Laboratories) and developed with DAB (Sigma Aldrich) according to the provider's instructions. To visualize dense core Aβ plaques, TREM2-labeled sections were counterstained with Congo red (Sigma Aldrich). To quantify the number of cells, sections were stained with hematoxylin and eosin (Vector Laboratories) following manufacturer's directions. Sections were dehydrated with increasing concentrations of ethanol, cleared with xylene, and cover-slipped with xylene-based mounting medium (Cytoseal XYL, Thermo Fisher Scientific). Sections were imaged with the Nikon Eclipse Ci microscope that was equipped with a DS-Ri2 camera and NIS-Elements Advanced Research imaging software (Nikon, Tokyo, Japan).

For immunofluorescence experiments, primary antibodies were detected with species-specific Alexa Fluor 488/568-coupled secondary antibodies (1:500, Thermo Fisher Scientific). Sections were mounted with aqueous mounting medium containing DAPI and anti-fading reagent (ProLong Gold Antifade Mountant, Invitrogen). Stained sections were analyzed by fluorescence confocal microscopy on a Nikon C2si laser scanning microscope that was equipped with NISElements Advanced Research software (Nikon, Tokyo, Japan).

For the assessment of Aβ plaque burden, four coronal sections spanning the cortex and hippocampus (at different depths on the rostro-caudal axis) were imaged for each animal. The amyloid plaque burden (area occupied by all plaques divided by the total area) was estimated in the cortex and hippocampus for each section using the Analyze Particles plugin of ImageJ software (NIH). Values from each section were averaged to generate a mean plaque burden for each animal.

For quantification of neuronal cell density, the cortical layer 5 and the CA1 area in the hippocampus were imaged at ×10 and ×20 magnifications, respectively. Two coronal sections spanning the cortex and hippocampus at different depths on the rostro-caudal axis were analyzed for each animal. Three images were acquired on matching areas of each the cortex and hippocampus per section. The number of neuronal cells (using NeuN labelling) was determined using the Cell Counter plugin of ImageJ and was divided by the area occupied by the cells. Values from each section were averaged to obtain a mean neuronal cell density for each animal.

For quantification of Caspase-3$^+$ cell density, the cortex and hippocampus were imaged at ×20 magnification. Two coronal sections spanning the cortex and hippocampus at different depths on the rostro-caudal axis were analyzed for each animal. Five to six images were acquired on matching areas of each the cortex and hippocampus per section. The number of Caspase-3$^+$ cells was determined using the Cell Counter plugin of ImageJ and was divided by the area occupied by the cells. Values from each section were averaged to obtain a mean Caspase-3$^+$ cell density for each animal.

To analyze the Iba1$^+$ cell response to Aβ plaques, coronal sections were stained with Iba1 and 3D6 for visualization of plaques, as described above. Three coronal sections spanning the cortex and hippocampus at different depths were analyzed for each animal. Images were acquired in random regions of the cortices and hippocampi at x20 magnification with the Nikon C2 confocal microscope. The number of Iba1$^+$ cells was determined using the Analyze Particles plugin of ImageJ and was divided by the area occupied by the cells. Values from each image were averaged to obtain a mean Iba1$^+$ cell density for each animal. For individual Aβ plaque analysis, images were acquired at x40 magnification and approximately 25 plaques were randomly selected and analyzed for each animal. The number of Iba1$^+$ cells was quantified within a 20 μm distance from the plaque by using the Cell Counter plugin of ImageJ. The distance between Iba1$^+$ cells and the center of their associated plaques was calculated using the Measure function of ImageJ. Surface are of the Iba1$^+$ cell body was measured using the Surface function of Imaris software (Bitplane). Area of the plaque was measured in the 3D6 channel using the Analyze Particles function of ImageJ. The number of TREM2$^+$ cells associated with Congo red-stained plaques was quantified using the Cell Counter plugin of ImageJ.

To analyze the colocalization between P2ry12$^+$ and Iba1$^+$ cells, coronal sections were stained with the anti-P2ry12 (red) and anti-Iba1 (green) antibodies, as described above. Two coronal sections spanning the cortex and hippocampus at different depths were analyzed for each animal. Five to six images were acquired on matching areas of each the cortex and hippocampus per section at x20 magnification with the Nikon C2 confocal microscope. The number of P2ry12$^+$Iba1$^+$ cells was determined using the Analyze Particles function of Image J and was divided by the area occupied by the cells. Values from each image were averaged to obtain a mean P2ry12$^+$Iba1$^+$ cell density for each animal. To determine the % P2ry12$^+$Iba1$^+$/Iba1$^+$ cells, the number of P2ry12$^+$Iba1$^+$ cells was divided by the total number of Iba1$^+$ cells and multiplied by 100%. The investigator was blind to the genotype for all the quantifications.

Mouse microglia isolation and FACS sorting—Mice were deeply anesthetized with CO_2 and transcardially perfused with 50 ml PBS/1 mM EDTA, and brains were removed from the skull. Brains (without the cerebellum) were rinsed in PBS and placed into a GentleMacs C-tube (Miltenyi Biotech) with pre-warmed RPMI 1640 medium (with L-glutamine, Gibco) containing Dispase (2 U/ml) and Collagenase Type 3 (200 U/ml, Worthington Biochemical Corporation) according to our previous protocol (Hickman et al., 2013). Brains (without cerebellum) from two mice of the same age, sex and genotype were pooled for each sorting experiment. Brains were dissociated using the GentleMACS Dissociator (Miltenyi Biotech) using the brain program settings and following

manufacturer's instruction. Brains were subjected to three rounds of dissociation, each followed by a period of incubation at 37 °C. After the second round of dissociation, DNase I grade II (Roche) was added to a final concentration of 40 U/ml and incubated at 37 °C. After the third round of dissociation, the enzymes were inactivated by adding PBS containing 2 mM EDTA and 5% fetal bovine serum. The brain tissue was triturated, passed through a 100-μm filter (Thermo Fisher Scientific) and centrifuged. Cell pellets were resuspended in 10.5 ml RPMI 1640 medium (Gibco), mixed gently with 4.5 ml physiologic Percoll (Sigma Aldrich), and centrifuged at 850 *g* for 40 minutes. Subsequently, cells were rinsed with PBS/1 mM EDTA and centrifuged at 500 *g* for 8 minutes. Contaminating red blood cells were lysed with Red blood cell lysing buffer (Sigma Aldrich) following manufacturer's directions. Cells were rinsed with PBS/1 mM EDTA and centrifuged at 500 *g* for 8 minutes. Cell pellets were resuspended in blocking buffer (PBS/1 mM EDTA/2% donkey serum) containing Fc block (1 μg/ml, anti-mouse CD16/32, clone 93, Biolegend) and incubated in ice for 10 minutes. Then, cells were labeled with Alexa647-anti-CD11b (5 μg/ml, clone M1/170, Biolegend) and Alexa488-anti-CD45 (5 μg/ml, clone 30-F11, Biolegend) antibodies for 30 minutes on ice. Cells were rinsed with PBS/1.0 mM EDTA/2% donkey serum and centrifuged at 400 *g* for 8 minutes. Cells were gently resuspended in PBS/1.0 mM EDTA and filtered into 5 ml polysterene filter top tubes (BD Falcon) for FACS. Cells were sorted based on CD11b/CD45 expression using FACS ARIA (BD Biosciences), as previously described (Hickman et al., 2013). FACS-sorted cells were centrifuged at 600 *g* for 10 minutes and cell pellets were used for RNA extraction.

RNA purification and mRNA sequencing—Microglial cell pellets were lysed in RLT-Plus buffer (Qiagen) containing 1% β-mercaptoethanol for RNA extraction. Cell lysates were transferred to QIAshredder (Qiagen) for homogenization and centrifuged at 18,000 *g* for 2 minutes. RNA was isolated from resulting cell lysates using the RNeasy Plus Micro Kit (Qiagen), following manufacturer's directions. During the RNA extraction protocol, samples were treated with RNase-free DNase I (Qiagen) directly on the RNeasy spin columns at room temperature for 15 minutes and washed with buffer RW1 (Qiagen). Each RNA sample was eluted in RNase-free water (15 μl, Qiagen) and RNA integrity was assessed with the Agilent RNA 6000 Pico Chip on the 2100 Bioanalyzer (Agilent). Purified RNA was quantified using the Qubit RNA High Sensitivity Assay Kit (Invitrogen) on the Qubit Fluorometer 3.0 (Thermo Fisher Scientific). Microglial RNA samples originating from mice of the same genotype, sex and age were pooled as needed to generate samples containing 100 ng of RNA. cDNA libraries were prepared using the TruSeq Stranded mRNA LT Prep Kit (Illumina) and following manufacturer's instruction. The protocol consisted of mRNA purification with poly-T oligo-attached magnetic beads, mRNA fragmentation, first and second strand cDNA synthesis, 3'end adenylation, adapter ligation, and PCR amplification (11 cycles). Libraries were enriched using the Agencourt AMPure XP beads (Beckman Coulter). cDNA libraries were validated using the Agilent DNA 1000 kit on the 2100 Bioanalyzer (Agilent) and quantified by qPCR before sequencing. Libraries were sequenced on a HiSeq 2500 instrument (Illumina) at the MGH Next Generation Sequencing Core Facility, using single-end 50 bp sequencing.

RNA-seq analysis—RNA sequencing resulted in 48.7 million reads per sample on average for the whole study. The splice-aware alignment program STAR was used to map sequencing reads (fastqs) to the mouse (mm10) reference genome. Gene expression counts were calculated using the program HTSeq based on the latest Ensembl annotation for mm10/GRCm38. The R package edgeR was used to make differential gene expression calls from these counts at a two-fold cut-off and false discovery rate (FDR)<0.05 threshold. Gene expression was considered upregulated if $\log_2$FC>1 or downregulated if $\log_2$FC<−1 [FC= fold-change of reads per kilobase per million (RPKMs)] at FDR<0.05.

Ingenuity Pathway Analysis—Data were analyzed with Ingenuity Pathway Analysis software (IPA, Qiagen). Differentially expressed genes (with corresponding fold changes and FDR values) were analyzed by IPA for canonical pathways. Briefly, data sets for analysis were filtered using the following cut-off definitions: two-fold change and FDR<0.05. Downregulated and upregulated gene data sets were uploaded separately and analyzed by IPA for canonical pathways. The Ingenuity Knowledge Base was used as the reference set in assembling pathways and relationship information derived from both human and mouse studies with experimentally observed confidence. IPA software also generated activation Z-scores: Z-score<−2 indicated that the pathway was inhibited, Z-score>2 indicated that the pathway was activated, at p-value<0.05.

Heatmaps—Visualization of single genotypes stemmed from a matrix of selected genes across individual samples using counts per million (CPM) expression values. A $\log_2$ transformation was applied to the matrix before being visualized using the heatmap.2 function from the gplots package in the R software for statistical computing. Negative and positive expression values were represented as z-scores ranging from −2 (blue) to 2 (red), respectively, and values were scaled per row to highlight differential expression across samples rather than the genes. Visualizations of multiple genotypes were generated in a similar fashion where one genotype dictated the genes of interest and individual RPKM expression values were organized into a matrix, transformed, and input into the previous function.

Heatmap visualization of CD33 and/or TREM2 dependency for the *5xFAD* versus WT dataset were computed using the $\log_2$FC values from experimental groups (no row rescaling) for the top 60 differentially expressed genes in the *5xFAD* versus WT dataset (p<0.001 and FDR<0.05). Dendrograms were computed by row using Euclidean distance and average linkage. Row color labels were applied for 8 groups.

Volcano plots—Dot plots visualizing the Log_2FC and $-\text{Log}_{10}$FDR of each gene were generated using the Bokeh plotting library written in Python. The horizontal dashed line shows where FDR=0.05 ($-\text{Log}_{10}\text{FDR}\approx 1.30$) on the y-axis, while the two vertical dashed lines show where $\text{Log}_2\text{FC}=-1$ (left) and $\text{Log}_2\text{FC}=1$ (right) on the x-axis. Genes with $\text{Log}_2\text{FC}>1$ and FDR<0.05 were filtered and represented in red, while genes with $\text{Log}_2\text{FC}<-1$ and FDR<0.05 were filtered and represented in blue.

Venn diagrams—Differentially expressed genes ($\text{Log}_2\text{FC}<-1$, $\text{Log}_2\text{FC}>1$ and FDR<0.05) were used to generate key overlapping genes by iterating over Ensembl gene IDs with

Python and exploring the intersection among different genotypes. Sets of overlapping genes were visualized using Venn diagrams that were generated in Adobe Photoshop.

Gene selection—To extract expression data for genes of interest, we used the Python Data Analysis Library (Pandas), a powerful tool for indexing and parsing large data frames.

STRING analysis—Known and potential protein-protein interactions of genes associated with inflammation-related pathways (identified by IPA) were mapped by using the Search Tool for the Retrieval of Interacting Genes/Proteins (STRING) software and database (version 10.5) with a medium confidence cut-off of 0.4. In the resulting protein association networks, proteins are shown as nodes, which are connected by lines whose thickness represents the confidence level. Thin lines connecting nodes represent “medium” confidence level in protein interaction, while thicker lines represent “high” and “highest” confidence level.

Gene Set Enrichment Analysis—Data were analyzed using the GSEA desktop application (v3.0) from the Broad Institute (Mootha et al., 2003; Subramanian et al., 2005). Gene set enrichment analysis (GSEA) was run for each experimental group separately: *5xFAD;CD33*$^{-/-}$ versus *5xFAD* and *5xFAD;TREM2*$^{-/-}$ versus *5xFAD*. The input data for the GSEA were the following: (1) a complete table of normalized gene expression values from each experimental group, (2) a mapping file for identifying probesets in ENSEMBL to Gene Symbols (ENSEMBL_mouse_gene.chip; GSEA desktop application v3.0), and (3) a database of gene sets from all 3 divisions of GO (biological process, molecular function, cellular component), annotations that have evidence code IEA (inferred from electronic annotation), and RCA (inferred from reviewed computational analysis; December 01, 2018 release; http://baderlab.org/GeneSets). A total of 7244 curated gene sets were included in the analysis. Inclusion gene set size was set between 15 and 500, and the gene set was permutated 1,000 times.

Enrichment maps were created using the EnrichmentMap plugin in Cytoscape (v3.7.0) for both experimental groups with a threshold p-value cutoff ($p<0.001$) and FDR q-value cutoff ($q<0.05$). 277 significant gene sets were enriched in the *5xFAD;CD33*$^{-/-}$ versus *5xFAD* group and 342 in the *5xFAD;TREM2*$^{-/-}$ versus *5xFAD* group. The enrichment maps were subsequently clustered and annotated using the AutoAnnotate plugin (Cytoscape v3.7.0).

Quantitative real-time PCR—Total RNA from FACS-sorted microglia was isolated using the RNeasy Plus Micro Kit (Qiagen) according to the manufacturer’s instructions. During the RNA extraction protocol, samples were treated with RNase-free DNase I (Qiagen). Purified RNA was quantified using the Qubit RNA High Sensitivity Assay Kit (Invitrogen) on the Qubit Fluorometer 3.0 (Thermo Fisher Scientific). The RNA was reverse-transcribed using the SuperScript III First Strand Synthesis System (Invitrogen). Gene expression was assessed by performing TaqMan real-time PCR assays. The probes targeting the *Il1b*, *Il1rn*, *Gpnmb*, and *Vegfa* genes were labeled with FAM (Thermo Fisher Scientific). The housekeeping gene *Gapdh* was used as control and the probe targeting *Gapdh* was labeled with VIC (Thermo Fisher Scientific). 1:10 diluted cDNAs were mixed with the probes and Taqman Universal Master Mix II (Applied Biosystems) and amplified

using the C1000 Touch Thermal Cycler (Bio-Rad). Results were analyzed by the comparative CT method. Average CT values for each sample were normalized to the average CT values of the housekeeping gene.

QUANTIFICATION AND STATISTICAL ANALYSIS

Statistics for transcriptomic analyses were described as above. For other quantitative results, statistical analysis was performed using the GraphPad Prism 7 (GraphPad Software). The normality of datasets was tested with the D'Agostino-Pearson omnibus test. Data from behavioral studies were analyzed by two-way ANOVA followed by Tukey's post-hoc test. Multiple group analyses were performed by one-way ANOVA followed by Tukey's post-hoc test for normally distributed datasets and by Kruskal-Wallis ANOVA followed by Dunn's post-hoc test otherwise. Unpaired t-test with Welch's correction was performed for normally distributed datasets and Mann-Whitney U test otherwise. All n and p-values and statistical tests are indicated in figure legends.

DATA AND SOFTWARE AVAILABILITY

The raw reads of the sequencing data are submitted to NCBI-GEO (GSE132508, "TREM2 Acts Downstream of CD33 in Modulating Microglial Pathology in Alzheimer's Disease").

Supplementary Material

Refer to Web version on PubMed Central for supplementary material.

Acknowledgements

The research was supported by grants from the NIA/NIH (K99AG049056 and 5R00AG049056 to AG, 5R01MH060009 to RET), Cure Alzheimer's Fund (AG, RET) and JPB Foundation (RET). JEK is supported by RF1 AG051506. We thank the MGH Next Generation Sequencing Core, Adalis Maisonet and Ulandt Kim for assistance in RNA-seq, and DF/HCC Pathology Core for assistance in histopathology.

References

Atagi Y, Liu CC, Painter MM, Chen XF, Verbeeck C, Zheng H, Li X, Rademakers R, Kang SS, Xu H, et al. (2015). Apolipoprotein E Is a Ligand for Triggering Receptor Expressed on Myeloid Cells 2 (TREM2). J Biol Chem 290, 26043–26050. [PubMed: 26374899]

Bailey CC, DeVaux LB, and Farzan M (2015). The Triggering Receptor Expressed on Myeloid Cells 2 Binds Apolipoprotein E. J Biol Chem 290, 26033–26042. [PubMed: 26374897]

Ben-Menachem-Zidon O, Ben-Menahem Y, Ben-Hur T, and Yirmiya R (2014). Intra-hippocampal transplantation of neural precursor cells with transgenic over-expression of IL-1 receptor antagonist rescues memory and neurogenesis impairments in an Alzheimer's disease model. Neuropsychopharmacology 39, 401–414. [PubMed: 23954849]

Bertram L, Lange C, Mullin K, Parkinson M, Hsiao M, Hogan MF, Schjeide BM, Hooli B, Divito J, Ionita I, et al. (2008). Genome-wide association analysis reveals putative Alzheimer's disease susceptibility loci in addition to APOE. Am J Hum Genet 83, 623–632. [PubMed: 18976728]

Bradshaw EM, Chibnik LB, Keenan BT, Ottoboni L, Raj T, Tang A, Rosenkrantz LL, Imboywa S, Lee M, Von Korff A, et al. (2013). CD33 Alzheimer's disease locus: altered monocyte function and amyloid biology. Nat Neurosci 16, 848–850. [PubMed: 23708142]

Chan G, White CC, Winn PA, Cimpean M, Replogle JM, Glick LR, Cuerdon NE, Ryan KJ, Johnson KA, Schneider JA, et al. (2015). CD33 modulates TREM2: convergence of Alzheimer loci. Nat Neurosci 18, 1556–1558. [PubMed: 26414614]

Crocker PR, Paulson JC, and Varki A (2007). Siglecs and their roles in the immune system. Nat Rev Immunol 7, 255–266. [PubMed: 17380156]

Efthymiou AG, and Goate AM (2017). Late onset Alzheimer's disease genetics implicates microglial pathways in disease risk. Mol Neurodegener 12, 43. [PubMed: 28549481]

Fernandez-Paredes L, Casrouge A, Decalf J, de Andres C, Villar LM, Perez de Diego R, Alonso B, Alvarez Cermeno JC, Arroyo R, Tejera-Alhambra M, et al. (2017). Multimarker risk stratification approach at multiple sclerosis onset. Clin Immunol 181, 43–50. [PubMed: 28578025]

Griciuc A, Serrano-Pozo A, Parrado AR, Lesinski AN, Asselin CN, Mullin K, Hooli B, Choi SH, Hyman BT, and Tanzi RE (2013). Alzheimer's disease risk gene CD33 inhibits microglial uptake of amyloid beta. Neuron 78, 631–643. [PubMed: 23623698]

Guerreiro R, Wojtas A, Bras J, Carrasquillo M, Rogaeva E, Majounie E, Cruchaga C, Sassi C, Kauwe JS, Younkin S, et al. (2013). TREM2 variants in Alzheimer's disease. N Engl J Med 368, 117–127. [PubMed: 23150934]

Hansen DV, Hanson JE, and Sheng M (2018). Microglia in Alzheimer's disease. J Cell Biol 217, 459–472. [PubMed: 29196460]

Heidary M, Rakhshi N, Pahlevan Kakhki M, Behmanesh M, Sanati MH, Sanadgol N, Kamaladini H, and Nikravesh A (2014). The analysis of correlation between IL-1B gene expression and genotyping in multiple sclerosis patients. J Neurol Sci 343, 41–45. [PubMed: 24867167]

Hendrickx DAE, van Scheppingen J, van der Poel M, Bossers K, Schuurman KG, van Eden CG, Hol EM, Hamann J, and Huitinga I (2017). Gene Expression Profiling of Multiple Sclerosis Pathology Identifies Early Patterns of Demyelination Surrounding Chronic Active Lesions. Front Immunol 8, 1810. [PubMed: 29312322]

Herran E, Perez-Gonzalez R, Igartua M, Pedraz JL, Carro E, and Hernandez RM (2013). VEGF-releasing biodegradable nanospheres administered by craniotomy: a novel therapeutic approach in the APP/Ps1 mouse model of Alzheimer's disease. J Control Release 170, 111–119. [PubMed: 23684689]

Hickman SE, Allison EK, and El Khoury J (2008). Microglial dysfunction and defective beta-amyloid clearance pathways in aging Alzheimer's disease mice. J Neurosci 28, 8354–8360. [PubMed: 18701698]

Hickman SE, Kingery ND, Ohsumi TK, Borowsky ML, Wang LC, Means TK, and El Khoury J (2013). The microglial sensome revealed by direct RNA sequencing. Nat Neurosci 16, 1896–1905. [PubMed: 24162652]

Hollingworth P, Harold D, Sims R, Gerrish A, Lambert JC, Carrasquillo MM, Abraham R, Hamshere ML, Pahwa JS, Moskvina V, et al. (2011). Common variants at ABCA7, MS4A6A/MS4A4E, EPHA1, CD33 and CD2AP are associated with Alzheimer's disease. Nat Genet 43, 429–435. [PubMed: 21460840]

Hu Y, Cao C, Qin XY, Yu Y, Yuan J, Zhao Y, and Cheng Y (2017). Increased peripheral blood inflammatory cytokine levels in amyotrophic lateral sclerosis: a meta-analysis study. Sci Rep 7, 9094. [PubMed: 28831083]

Ishida A, Akita K, Mori Y, Tanida S, Toda M, Inoue M, and Nakada H (2014). Negative regulation of Toll-like receptor-4 signaling through the binding of glycosylphosphatidylinositol-anchored glycoprotein, CD14, with the sialic acid-binding lectin, CD33. J Biol Chem 289, 25341–25350. [PubMed: 25059667]

Jay TR, Hirsch AM, Broihier ML, Miller CM, Neilson LE, Ransohoff RM, Lamb BT, and Landreth GE (2017). Disease Progression-Dependent Effects of TREM2 Deficiency in a Mouse Model of Alzheimer's Disease. J Neurosci 37, 637–647. [PubMed: 28100745]

Jay TR, Miller CM, Cheng PJ, Graham LC, Bemiller S, Broihier ML, Xu G, Margevicius D, Karlo JC, Sousa GL, et al. (2015). TREM2 deficiency eliminates TREM2+ inflammatory macrophages and ameliorates pathology in Alzheimer's disease mouse models. J Exp Med 212, 287–295. [PubMed: 25732305]

Jonsson T, Stefansson H, Steinberg S, Jonsdottir I, Jonsson PV, Snaedal J, Bjornsson S, Huttenlocher J, Levey AI, Lah JJ, et al. (2013). Variant of TREM2 associated with the risk of Alzheimer's disease. N Engl J Med 368, 107–116. [PubMed: 23150908]

Karch CM, Jeng AT, Nowotny P, Cady J, Cruchaga C, and Goate AM (2012). Expression of novel Alzheimer's disease risk genes in control and Alzheimer's disease brains. PLoS One 7, e50976. [PubMed: 23226438]

Keren-Shaul H, Spinrad A, Weiner A, Matcovitch-Natan O, Dvir-Szternfeld R, Ulland TK, David E, Baruch K, Lara-Astaiso D, Toth B, et al. (2017). A Unique Microglia Type Associated with Restricting Development of Alzheimer's Disease. Cell 169, 1276–1290 e1217. [PubMed: 28602351]

Krasemann S, Madore C, Cialic R, Baufeld C, Calcagno N, El Fatimy R, Beckers L, O'Loughlin E, Xu Y, Fanek Z, et al. (2017). The TREM2-APOE Pathway Drives the Transcriptional Phenotype of Dysfunctional Microglia in Neurodegenerative Diseases. Immunity 47, 566–581 e569. [PubMed: 28930663]

Lee CYD, Daggett A, Gu X, Jiang LL, Langfelder P, Li X, Wang N, Zhao Y, Park CS, Cooper Y, et al. (2018). Elevated TREM2 Gene Dosage Reprograms Microglia Responsivity and Ameliorates Pathological Phenotypes in Alzheimer's Disease Models. Neuron 97, 1032–1048 e1035. [PubMed: 29518357]

Lessard CB, Malnik SL, Zhou Y, Ladd TB, Cruz PE, Ran Y, Mahan TE, Chakrabaty P, Holtzman DM, Ulrich JD, et al. (2018). High-affinity interactions and signal transduction between Abeta oligomers and TREM2. EMBO Mol Med 10.

Leyns CEG, Ulrich JD, Finn MB, Stewart FR, Koscal LJ, Remolina Serrano J, Robinson GO, Anderson E, Colonna M, and Holtzman DM (2017). TREM2 deficiency attenuates neuroinflammation and protects against neurodegeneration in a mouse model of tauopathy. Proc Natl Acad Sci U S A 114, 11524–11529. [PubMed: 29073081]

Li B, Castano AP, Hudson TE, Nowlin BT, Lin SL, Bonventre JV, Swanson KD, and Duffield JS (2010). The melanoma-associated transmembrane glycoprotein Gpnmb controls trafficking of cellular debris for degradation and is essential for tissue repair. FASEB J 24, 4767–4781. [PubMed: 20709912]

Malik M, Simpson JF, Parikh I, Wilfred BR, Fardo DW, Nelson PT, and Estus S (2013). CD33 Alzheimer's risk-altering polymorphism, CD33 expression, and exon 2 splicing. J Neurosci 33, 13320–13325. [PubMed: 23946390]

Merico D, Isserlin R, Stueker O, Emili A, and Bader GD (2010). Enrichment map: a network-based method for gene-set enrichment visualization and interpretation. PLoS One 5, e13984. [PubMed: 21085593]

Mootha VK, Lindgren CM, Eriksson KF, Subramanian A, Sihag S, Lehar J, Puigserver P, Carlsson E, Ridderstrale M, Laurila E, et al. (2003). PGC-1alpha-responsive genes involved in oxidative phosphorylation are coordinately downregulated in human diabetes. Nat Genet 34, 267–273. [PubMed: 12808457]

Naj AC, Jun G, Beecham GW, Wang LS, Vardarajan BN, Buros J, Gallins PJ, Buxbaum JD, Jarvik GP, Crane PK, et al. (2011). Common variants at MS4A4/MS4A6E, CD2AP, CD33 and EPHA1 are associated with late-onset Alzheimer's disease. Nat Genet 43, 436–441. [PubMed: 21460841]

Oakley H, Cole SL, Logan S, Maus E, Shao P, Craft J, Guillozet-Bongaarts A, Ohno M, Disterhoft J, Van Eldik L, et al. (2006). Intraneuronal beta-amyloid aggregates, neurodegeneration, and neuron loss in transgenic mice with five familial Alzheimer's disease mutations: potential factors in amyloid plaque formation. J Neurosci 26, 10129–10140. [PubMed: 17021169]

Pasquarella C, Veronesi L, Napoli C, Castiglia P, Liguori G, Rizzetto R, Torre I, Righi E, Farruggia P, Tesauro M, et al. (2012). Microbial environmental contamination in Italian dental clinics: A multicenter study yielding recommendations for standardized sampling methods and threshold values. Sci Total Environ 420, 289–299. [PubMed: 22335883]

Son M, Diamond B, Volpe BT, Aranow CB, Mackay MC, and Santiago-Schwarz F (2017). Evidence for C1q-mediated crosslinking of CD33/LAIR-1 inhibitory immunoreceptors and biological control of CD33/LAIR-1 expression. Sci Rep 7, 270. [PubMed: 28325905]

Song W, Hooli B, Mullin K, Jin SC, Cella M, Ulland TK, Wang Y, Tanzi RE, and Colonna M (2017). Alzheimer's disease-associated TREM2 variants exhibit either decreased or increased ligand-dependent activation. Alzheimers Dement 13, 381–387. [PubMed: 27520774]

Song WM, Joshita S, Zhou Y, Ulland TK, Gilfillan S, and Colonna M (2018). Humanized TREM2 mice reveal microglia-intrinsic and -extrinsic effects of R47H polymorphism. J Exp Med 215, 745–760. [PubMed: 29321225]

Suarez-Calvet M, Kleinberger G, Araque Caballero MA, Brendel M, Rominger A, Alcolea D, Fortea J, Lleo A, Blesa R, Gispert JD, et al. (2016). sTREM2 cerebrospinal fluid levels are a potential biomarker for microglia activity in early-stage Alzheimer's disease and associate with neuronal injury markers. EMBO Mol Med 8, 466–476. [PubMed: 26941262]

Subramanian A, Tamayo P, Mootha VK, Mukherjee S, Ebert BL, Gillette MA, Paulovich A, Pomeroy SL, Golub TR, Lander ES, et al. (2005). Gene set enrichment analysis: a knowledge-based approach for interpreting genome-wide expression profiles. Proc Natl Acad Sci U S A 102, 15545–15550. [PubMed: 16199517]

Takahashi K, Rochford CD, and Neumann H (2005). Clearance of apoptotic neurons without inflammation by microglial triggering receptor expressed on myeloid cells-2. J Exp Med 201, 647–657. [PubMed: 15728241]

Tanaka H, Shimazawa M, Kimura M, Takata M, Tsuruma K, Yamada M, Takahashi H, Hozumi I, Niwa J, Iguchi Y, et al. (2012). The potential of GPNMB as novel neuroprotective factor in amyotrophic lateral sclerosis. Sci Rep 2, 573. [PubMed: 22891158]

Tanzi RE (2012). The genetics of Alzheimer disease. Cold Spring Harb Perspect Med 2.

Tanzi RE (2015). TREM2 and Risk of Alzheimer's Disease--Friend or Foe? N Engl J Med 372, 2564–2565. [PubMed: 26107057]

Turnbull IR, Gilfillan S, Cella M, Aoshi T, Miller M, Piccio L, Hernandez M, and Colonna M (2006). Cutting edge: TREM-2 attenuates macrophage activation. J Immunol 177, 3520–3524. [PubMed: 16951310]

Ulland TK, Song WM, Huang SC, Ulrich JD, Sergushichev A, Beatty WL, Loboda AA, Zhou Y, Cairns NJ, Kambal A, et al. (2017). TREM2 Maintains Microglial Metabolic Fitness in Alzheimer's Disease. Cell 170, 649–663 e613. [PubMed: 28802038]

Ulrich JD, Finn MB, Wang Y, Shen A, Mahan TE, Jiang H, Stewart FR, Piccio L, Colonna M, and Holtzman DM (2014). Altered microglial response to Abeta plaques in APPPS1–21 mice heterozygous for TREM2. Mol Neurodegener 9, 20. [PubMed: 24893973]

Vorhees CV, and Williams MT (2006). Morris water maze: procedures for assessing spatial and related forms of learning and memory. Nat Protoc 1, 848–858. [PubMed: 17406317]

Walker DG, Whetzel AM, Serrano G, Sue LI, Beach TG, and Lue LF (2015). Association of CD33 polymorphism rs3865444 with Alzheimer's disease pathology and CD33 expression in human cerebral cortex. Neurobiol Aging 36, 571–582. [PubMed: 25448602]

Wang Y, Cella M, Mallinson K, Ulrich JD, Young KL, Robinette ML, Gilfillan S, Krishnan GM, Sudhakar S, Zinselmeyer BH, et al. (2015). TREM2 lipid sensing sustains the microglial response in an Alzheimer's disease model. Cell 160, 1061–1071. [PubMed: 25728668]

Wang Y, Ulland TK, Ulrich JD, Song W, Tzaferis JA, Hole JT, Yuan P, Mahan TE, Shi Y, Gilfillan S, et al. (2016). TREM2-mediated early microglial response limits diffusion and toxicity of amyloid plaques. J Exp Med 213, 667–675. [PubMed: 27091843]

Yeh FL, Hansen DV, and Sheng M (2017). TREM2, Microglia, and Neurodegenerative Diseases. Trends Mol Med 23, 512–533. [PubMed: 28442216]

Yeh FL, Wang Y, Tom I, Gonzalez LC, and Sheng M (2016). TREM2 Binds to Apolipoproteins, Including APOE and CLU/APOJ, and Thereby Facilitates Uptake of Amyloid-Beta by Microglia. Neuron 91, 328–340. [PubMed: 27477018]

Yuan P, Condello C, Keene CD, Wang Y, Bird TD, Paul SM, Luo W, Colonna M, Baddeley D, and Grutzendler J (2016). TREM2 Haplodeficiency in Mice and Humans Impairs the Microglia Barrier Function Leading to Decreased Amyloid Compaction and Severe Axonal Dystrophy. Neuron 90, 724–739. [PubMed: 27196974]

Zhao Y, Wu X, Li X, Jiang LL, Gui X, Liu Y, Sun Y, Zhu B, Pina-Crespo JC, Zhang M, et al. (2018). TREM2 Is a Receptor for beta-Amyloid that Mediates Microglial Function. Neuron 97, 1023–1031 e1027. [PubMed: 29518356]

Zhong L, Wang Z, Wang D, Wang Z, Martens YA, Wu L, Xu Y, Wang K, Li J, Huang R, et al. (2018). Amyloid-beta modulates microglial responses by binding to the triggering receptor expressed on myeloid cells 2 (TREM2). Mol Neurodegener 13, 15. [PubMed: 29587871]

Highlights

- Mitigation of Aβ pathology in *5xFAD;CD33*$^{-/-}$ mice is abrogated by knocking out *TREM2*
- Reduction of Iba1^{+} cells in *5xFAD;TREM2*$^{-/-}$ mice is not rescued by knocking out *CD33*
- *CD33* and *TREM2* knock-out increase and reduce microglial activation, respectively
- Gene expression changes in *5xFAD;CD33*$^{-/-}$ microglia depend on the presence of *TREM2*

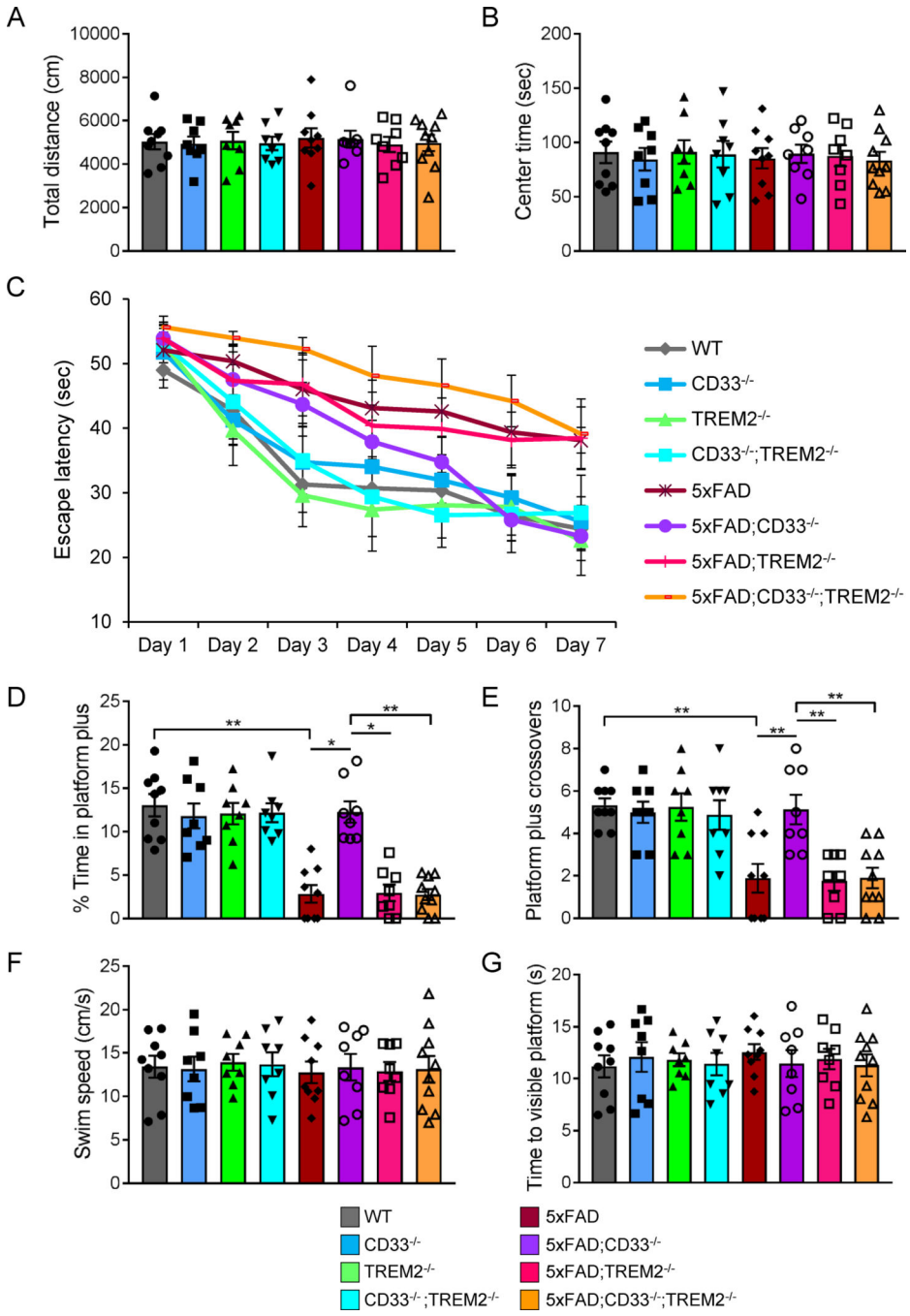

Figure 1. *CD33* knock-out restores retention memory in *5xFAD* mice, which is abrogated by additional knock-out of *TREM2*.

7-month-old WT (n=5M/4F), *CD33*$^{-/-}$ (n=4M/4F), *TREM2*$^{-/-}$ (n=4M/4F), *CD33*$^{-/-}$*;TREM2*$^{-/-}$ (n=4M/4F), *5xFAD* (n=5M/4F), *5xFAD;CD33*$^{-/-}$ (n=4M/4F), *5xFAD;TREM2*$^{-/-}$ (n=4M/4F) and *5xFAD;CD33*$^{-/-}$*;TREM2*$^{-/-}$ (n=5M/5F) mice were evaluated in the open field (A and B) and Morris water maze (C-G) tests. (A and B) All mouse genotypes were characterized by similar total distance moved (A, Kruskal-Wallis ANOVA, Dunn's test) and time spent in the center area (B, one-way ANOVA, Tukey's test). (C) Time needed to reach the hidden platform was plotted across training days. A two-way

repeated measures ANOVA revealed significant effects for days ($F_{(6,360)}$=71.24, p<0.0001) and for groups ($F_{(7,60)}$=5.781, p<0.0001), but not for interaction ($F_{(42,360)}$=1.407, p=0.0539). Two-way ANOVA, Tukey's test revealed a difference in *5xFAD;CD33*$^{-/-}$ mice versus *5xFAD;CD33*$^{-/-}$*;TREM2*$^{-/-}$ on days 6 (p<0.01) and 7 (p<0.05). (D and E) Time spent by the mice in the area surrounding the platform location (platform plus, D) and the number of platform plus crossovers (E) were recorded during the probe test (day 8). For (D), *p<0.05, **p<0.01, Kruskal-Wallis ANOVA (p<0.0001), Dunn's test. For (E), **p<0.01, one-way ANOVA ($F_{(7,60)}$=9.134, p<0.0001), Tukey's test. (F) All mouse groups showed similar swim speed during the test (one-way ANOVA, Tukey's test). (G) On days 9 and 10, no differences in latencies to the visible platform were found among mouse groups (one-way ANOVA, Tukey's test). Data are represented as mean ± SEM. See also Figure S1.

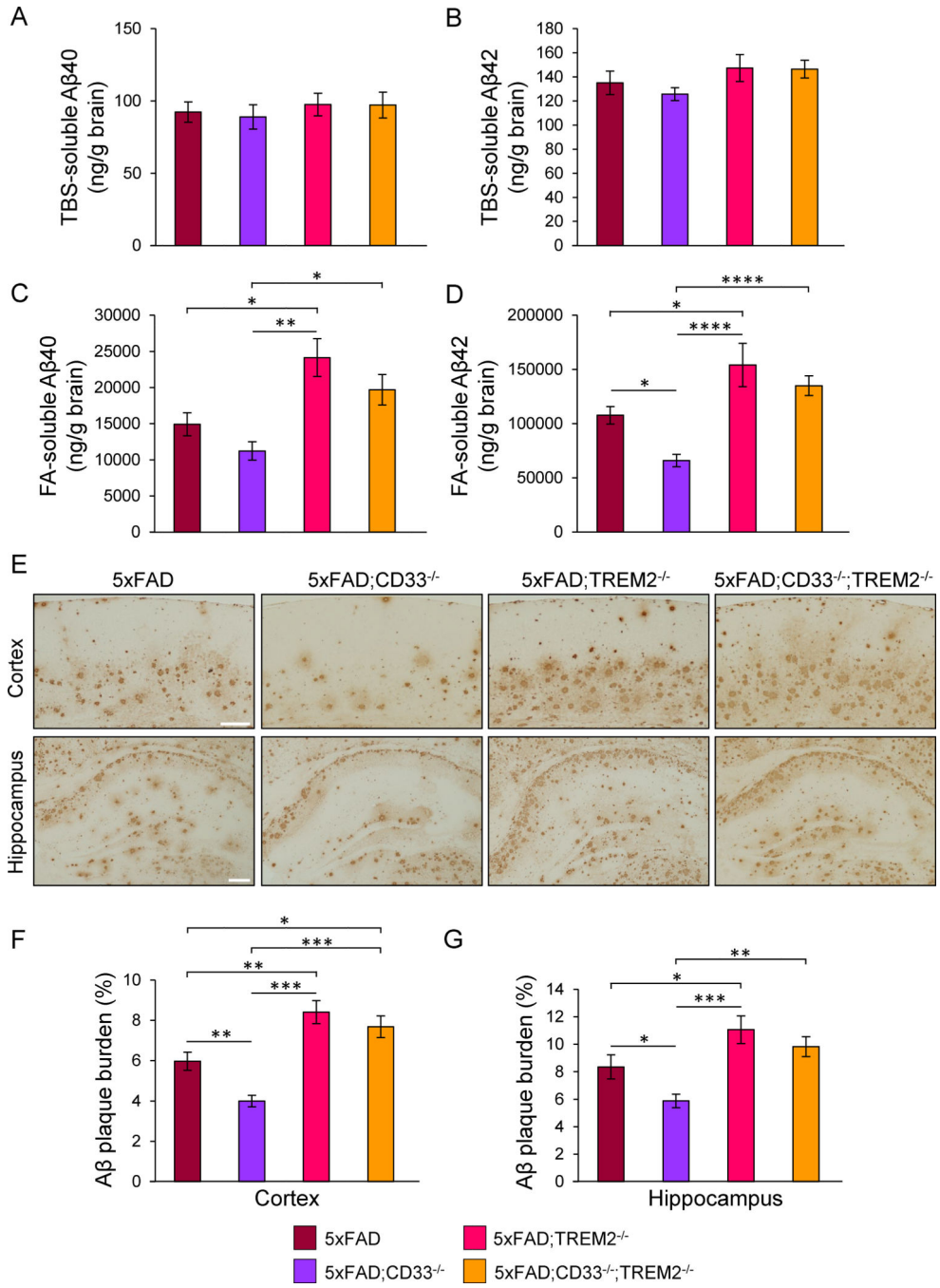

Figure 2. *CD33* knock-out leads to decreased levels of formic acid-soluble Aβ42 and Aβ plaque burden, abolished by additional knock-out of *TREM2*.

(A–D) ELISA analysis of Aβ40 (A and C) and Aβ42 (B and D) in TBS-soluble (A and B) and formic acid (FA)-soluble (C and D) fractions isolated from the cortex of 8-month-old mice. (E) Images of cortical and hippocampal fields from mice of indicated genotypes, labeled with the anti-Aβ antibody 3D6. Scale bar represents 100 μm. (F and G) Quantification of amyloid plaque burden in cortex (F) and hippocampus (G) of 8-month-old mice. For (A)-(G), *p<0.05, **p<0.01, ***p<0.001, ****p<0.0001, one-way ANOVA, Tukey's test, *5xFAD* (n=7M/7F), *5xFAD;CD33*$^{-/-}$ (n=7M/7F), *5xFAD;TREM2*$^{-/-}$

(n=4M/4F) and *5xFAD;CD33*$^{-/-}$*;TREM2*$^{-/-}$ (n=5M/6F) mice. Data are represented as mean ± SEM. See also Figure S2.

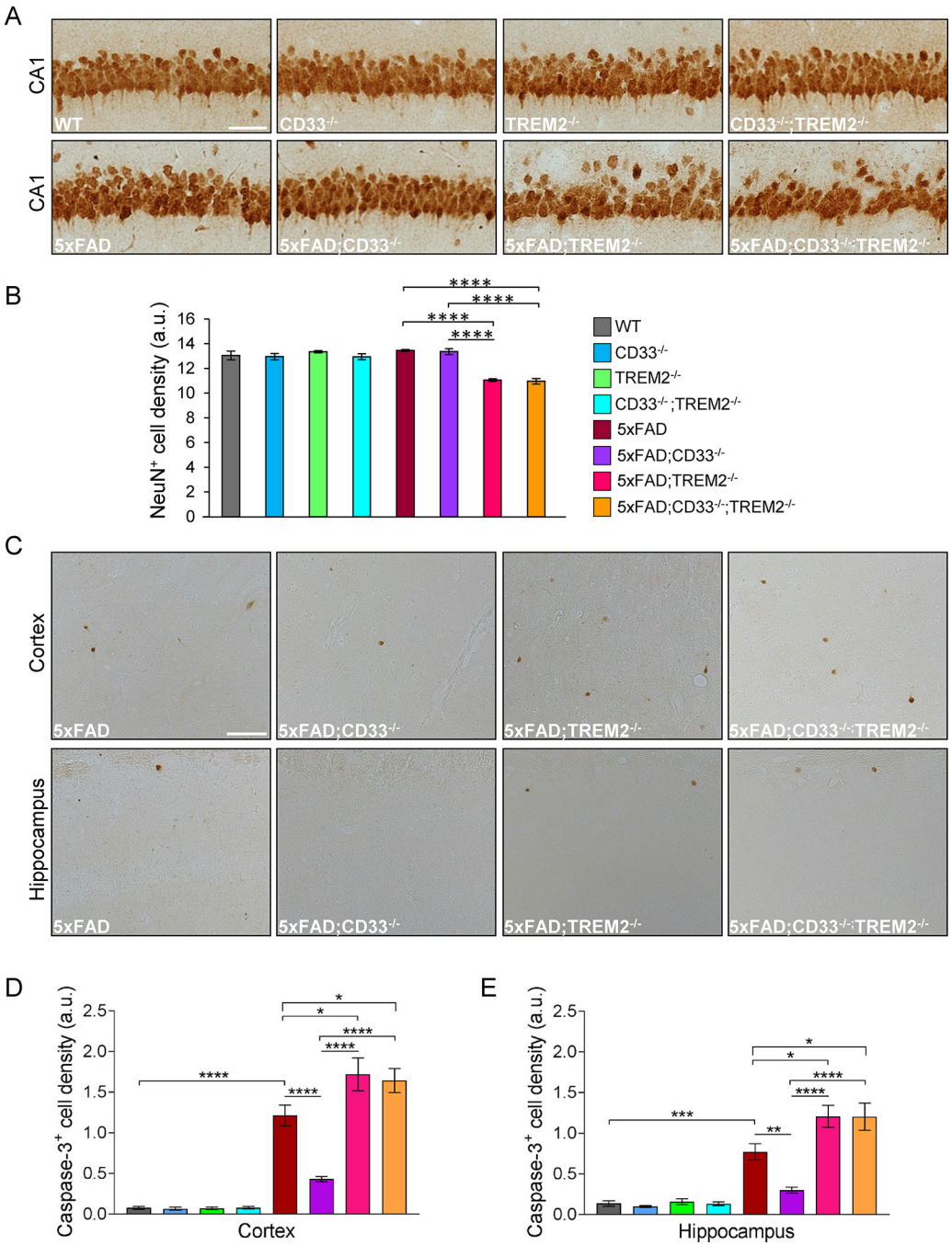

Figure 3. *TREM2* knock-out leads to neuronal cell loss in *5xFAD* mice, which is not rescued by additional knock-out of *CD33*.

(A) Representative pictures from CA1 of 8-month-old mice of indicated genotypes, labeled with anti-NeuN antibody. Scale bar represents 50 μm. (B) Summary of $NeuN^+$ cell numbers in CA1 of 8-month-old mice. (C) Representative images from the cortex and hippocampus of 8-month-old mice of indicated genotypes, labeled with an antibody against activated Caspase-3. Scale bar represents 50 μm. (D and E) Quantification of Caspase-3^+ cells in cortex (D) and hippocampus (E) of 8-month-old mice. For (B), (D) and (E), *p<0.05, **p<0.01, ***p<0.001, ****p<0.0001, one-way ANOVA, Tukey's test, WT (n=4M/4F),

CD33$^{-/-}$ (n=4M/4F), *TREM2*$^{-/-}$ (n=4M/4F), *CD33*$^{-/-}$;*TREM2*$^{-/-}$ (n=4M/4F), *5xFAD* (n=7M/7F), *5xFAD;CD33*$^{-/-}$ (n=7M/7F), *5xFAD;TREM2*$^{-/-}$ (n=4M/4F) and *5xFAD;CD33*$^{-/-}$;*TREM2*$^{-/-}$ (n=5M/6F) mice. Data are represented as mean ± SEM. See also Figure S3.

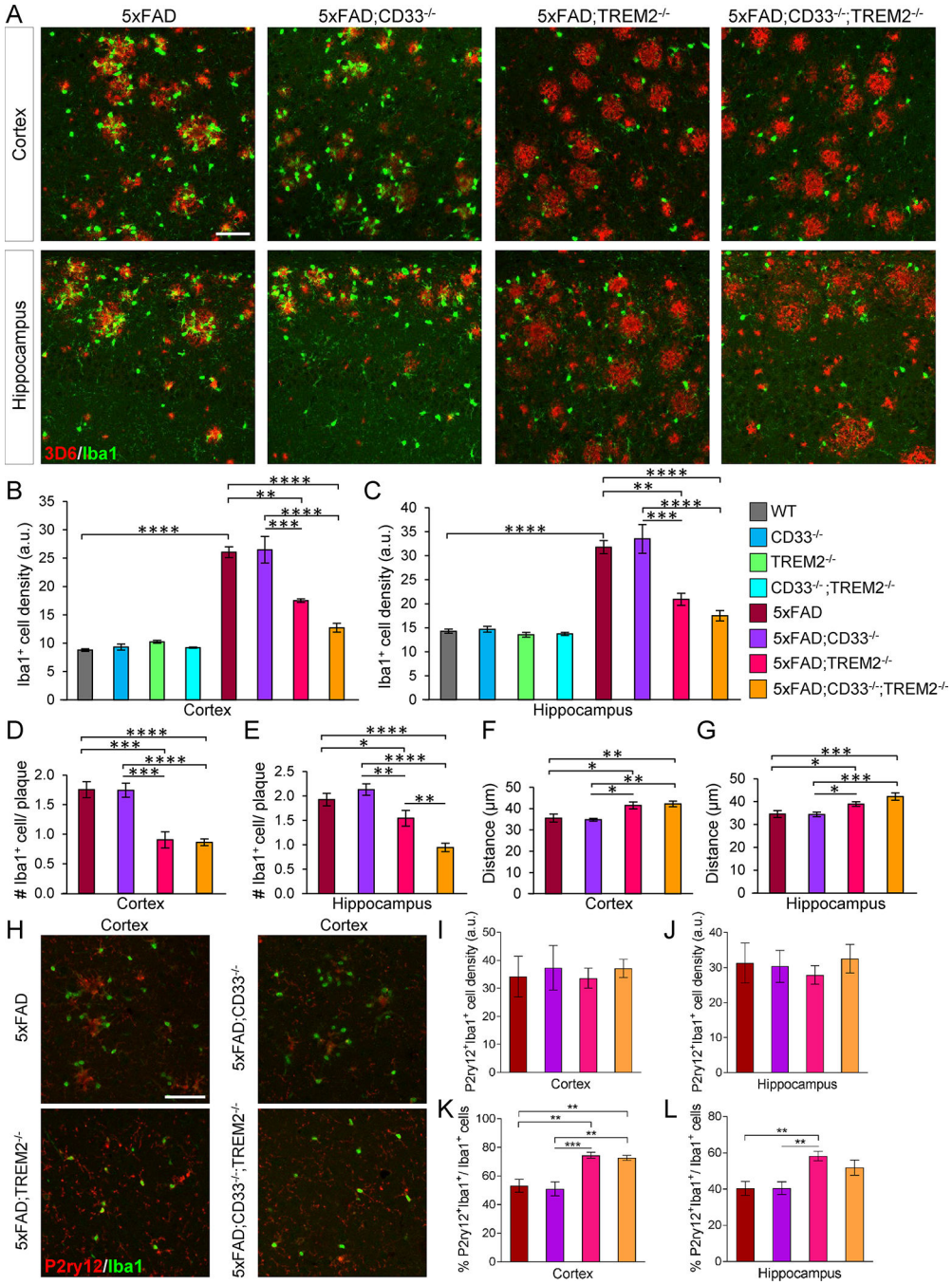

Figure 4. *TREM2* knock-out leads to reduced Iba1$^+$ cell numbers and clustering of Iba1$^+$ cells around Aβ plaques in *5xFAD* mice, both of which are not rescued by additional knock-out of *CD33*.

(A) Brain sections were labeled with Iba1 (green) and 3D6 antibody (red) for Aβ plaques. Representative images of cortex and hippocampus from of 8-month-old mice of indicated genotypes. Scale bar represents 50 µm. (B and C) Quantification of Iba1$^+$ cells in cortex (B) and hippocampus (C). (D and E) Quantification of Iba1$^+$ cells associated with plaques of similar sizes in cortex (D) and hippocampus (E). (F and G) Plaque-associated Iba1$^+$ cells were analyzed for their distance from the center of adjacent plaque in cortex (F) and

hippocampus (G). For (B)-(G), *p<0.05, **p<0.01, ***p<0.001, ****p<0.0001, one-way ANOVA, Tukey's test, 8-month-old WT (n=4M/4F), *CD33*$^{-/-}$ (n=4M/4F), *TREM2*$^{-/-}$ (n=4M/4F), *CD33*$^{-/-}$*;TREM2*$^{-/-}$ (n=4M/4F), *5xFAD* (n=7M/7F), *5xFAD;CD33*$^{-/-}$ (n=7M/7F), *5xFAD;TREM2*$^{-/-}$ (n=4M/4F) and *5xFAD;CD33*$^{-/-}$*;TREM2*$^{-/-}$ (n=5M/6F) mice. (H) Images from the cortex of 8-month-old mice of indicated genotypes, stained with P2ry12 (red) and Iba1-specific antibody (green). Scale bar represents 50 μm. (I and J) Quantification of P2ry12^{+}Iba1^{+} cells in cortex (I) and hippocampus (J) of 8-month-old mice. (K and L) Quantification of % P2ry12^{+}Iba1^{+}/Iba1^{+} cells in cortex (K) and hippocampus (L) of 8-month-old mice. For (I)-(L), **p<0.01, ***p<0.001, one-way ANOVA, Tukey's test, *5xFAD* (n=4M/4F), *5xFAD;CD33*$^{-/-}$ (n=4M/4F), *5xFAD;TREM2*$^{-/-}$ (n=4M/4F) and *5xFAD;CD33*$^{-/-}$*;TREM2*$^{-/-}$ (n=4M/4F) mice. Data are represented as mean ± SEM. See also Figure S4.

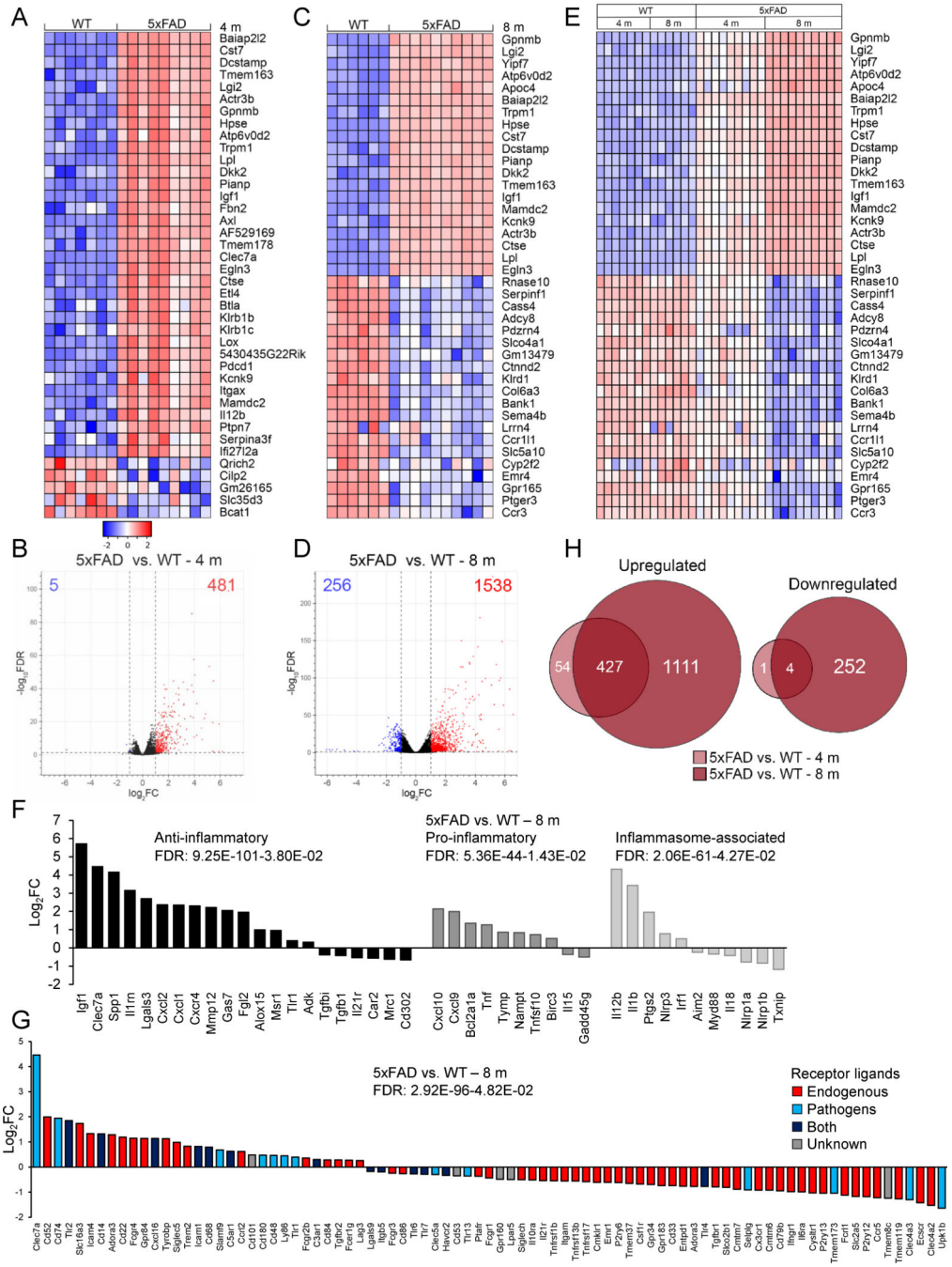

Figure 5. The microglial transcriptome changes in a progressive, age-dependent manner in *5xFAD* mice.

(A) Expression heatmap of top 40 DE genes in 4-month-old *5xFAD* microglia compared to WT by RNA-seq. Genes were ranked by FC; samples were grouped by genotype (WT: n=13M/14F, *5xFAD*: n=14M/14F mice). (B) Corresponding volcano plot of *5xFAD* microglia versus WT showed 481 upregulated ($log_2FC>1$, FDR<0.05, red) and 5 downregulated ($log_2FC<-1$, FDR<0.05, blue) genes. (C) Expression heatmap of top 40 DE genes in 8-month-old *5xFAD* microglia compared to WT, ranked by FC, and grouped by genotype (WT: n=8M/8F, *5xFAD*: n=10M/9F mice). (D) Corresponding volcano plot of

5xFAD microglia relative to WT. (E) Heatmap of top 40 DE genes in 8 and 4-month-old *5xFAD* microglia compared to WT, ranked by FC of 8-month-old *5xFAD* versus WT, grouped by genotype and time point. (F) Anti-inflammatory, pro-inflammatory and inflammasome-associated genes were concurrently upregulated in 8-month-old *5xFAD* microglia versus WT. (G) Genes related to pathogen sensing and host defense (*Clec7a*→*C5ar1*, blue and navy bars) were upregulated in 8-month-old *5xFAD* mice compared to WT. Genes related to sensing endogenous ligands (*Siglech*→*Clec4a2*, red bars) were downregulated. (H) Upregulated (left) or downregulated (right) genes in *5xFAD* microglia versus WT at each time point, displayed as Venn diagrams. See also Tables S1 and S2.

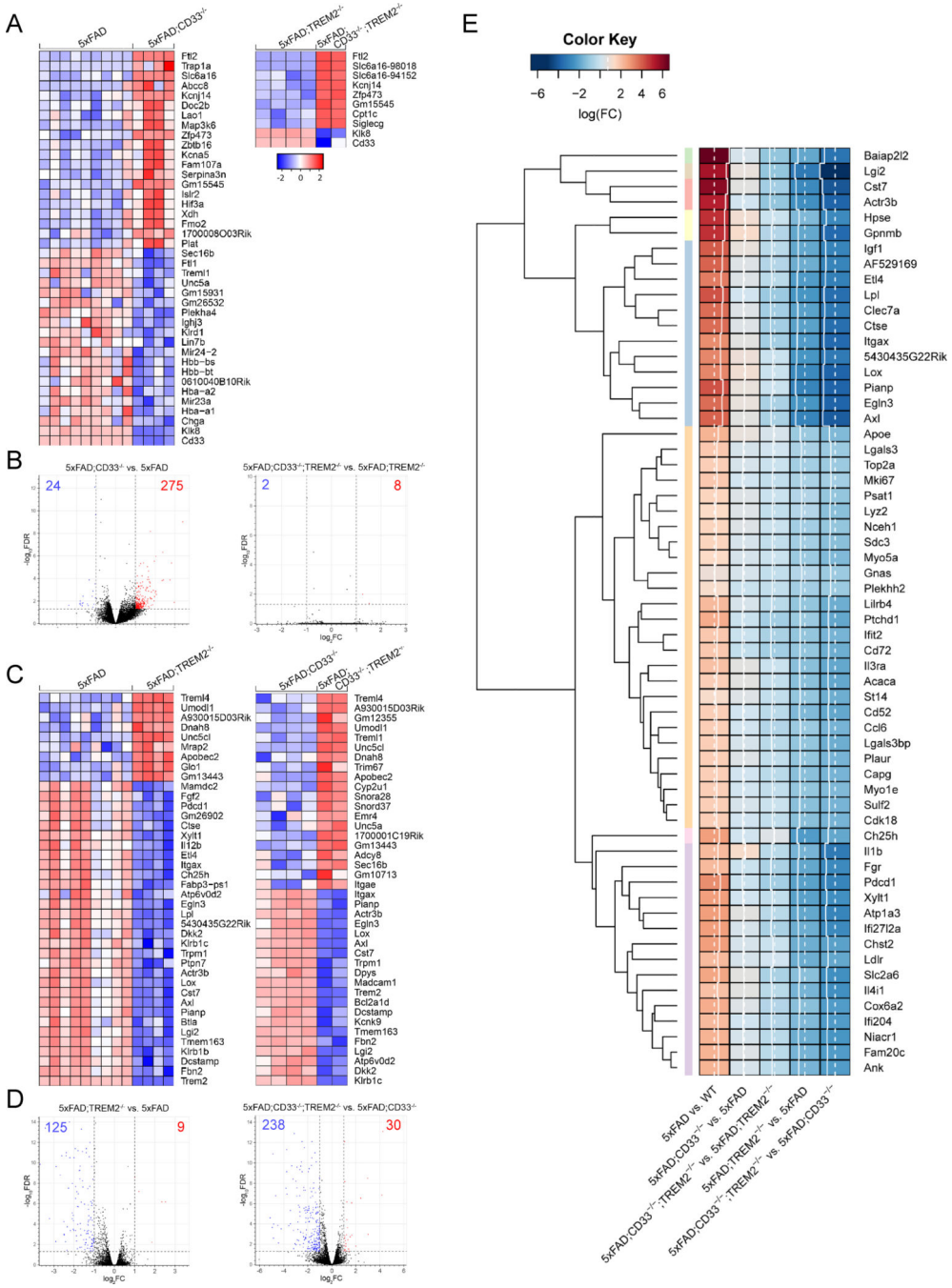

Figure 6. Differential gene expression in *5xFAD;CD33*$^{-/-}$ microglia is contingent upon the presence of *TREM2*, but this is not the case for *CD33* in *5xFAD;TREM2*$^{-/-}$ microglia.

(A) Expression heatmap of top 40 DE genes in 4-month-old *5xFAD;CD33*$^{-/-}$ microglia compared to *5xFAD* (left) and *5xFAD;CD33*$^{-/-}$;*TREM2*$^{-/-}$ relative to *5xFAD;TREM2*$^{-/-}$ (right). Genes were ranked by FC; samples were grouped by genotype (*5xFAD*: n=14M/14F, *5xFAD;CD33*$^{-/-}$: n=6M/6F, *5xFAD;TREM2*$^{-/-}$: n=11M/11F and *5xFAD;CD33*$^{-/-}$;*TREM2*$^{-/-}$: n=5M/5F mice). (B) Volcano plot of *5xFAD;CD33*$^{-/-}$ microglia in the presence of *TREM2* (left) showed 24 downregulated ($\log_2$FC<−1, FDR<0.05, blue) and 275 upregulated ($\log_2$FC>1, FDR<0.05, red) genes. Volcano plot of

5xFAD;CD33$^{-/-}$ microglia in the absence of *TREM2* (right) yielded only 2 downregulated and 8 upregulated genes. (C) Expression heatmap of top 40 DE genes in 4-month-old *5xFAD;TREM2*$^{-/-}$ microglia versus *5xFAD* (left) and *5xFAD;CD33*$^{-/-}$;*TREM2*$^{-/-}$ compared to *5xFAD;CD33*$^{-/-}$ (right). (D) Volcano plot of *5xFAD;TREM2*$^{-/-}$ microglia in the presence of *CD33* (left) showed 125 downregulated and 9 upregulated genes. Volcano plot of *5xFAD;TREM2*$^{-/-}$ in the absence of *CD33* (right) yielded 238 downregulated and 30 upregulated genes. (E) Top 60 DE genes (p-value<0.001 and FDR<0.05) in *5xFAD* versus WT were selected and corresponding $\log_2$FC values were hierarchically clustered (euclidean distance, average linkage) across the datasets: *5xFAD;CD33*$^{-/-}$ versus *5xFAD*, *5xFAD;CD33*$^{-/-}$;*TREM2*$^{-/-}$ versus *5xFAD;TREM2*$^{-/-}$, *5xFAD;TREM2*$^{-/-}$ versus *5xFAD*, and *5xFAD;CD33*$^{-/-}$;*TREM2*$^{-/-}$ versus *5xFAD;CD33*$^{-/-}$. The heatmap is presented with row dendrograms and cluster membership (by row color). See also Figures S5, S6 and Tables S2 and S3.

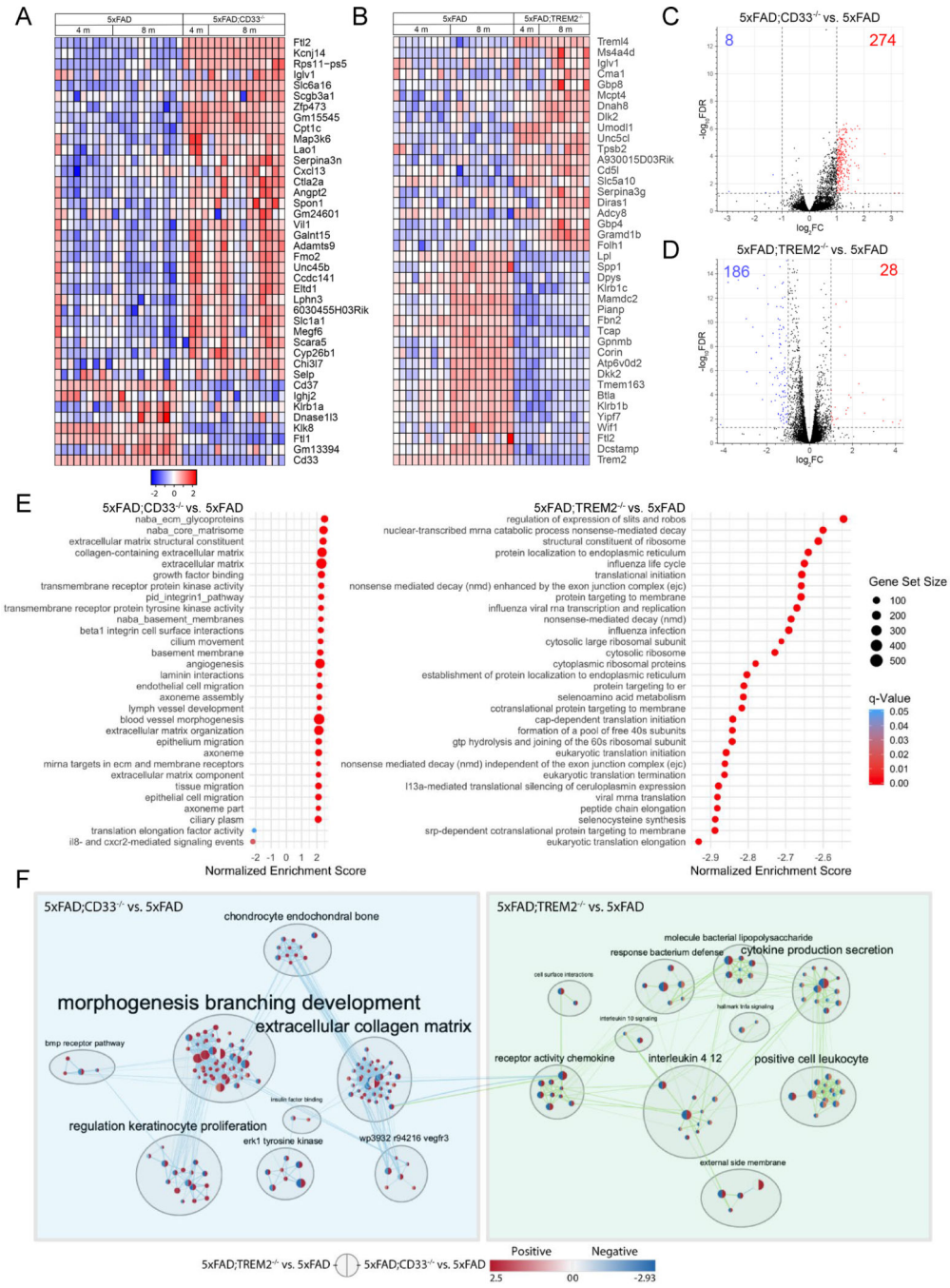

Figure 7. Crosstalk between CD33 and TREM2 in *5xFAD* microglia includes regulation of gene sets related to the extracellular collagen matrix and receptor activity chemokine clusters.

(A) Expression heatmap of top 40 DE genes in 8-month-old *5xFAD;CD33*$^{-/-}$ microglia that were also DE in 4-month-old *5xFAD;CD33*$^{-/-}$ (compared to *5xFAD*). Genes were ranked by FC of 8-month-old *5xFAD;CD33*$^{-/-}$ versus *5xFAD*; samples were grouped by genotype and time point (*5xFAD*: n=14M/14F, *5xFAD;CD33*$^{-/-}$: n=6M/6F at 4 months; and *5xFAD*: n=12M/12F, *5xFAD;CD33*$^{-/-}$: n=13M/13F mice at 8 months). (B) Heatmap of top 40 DE genes in 8-month-old *5xFAD;TREM2*$^{-/-}$ microglia that were also DE in 4-month-old *5xFAD;TREM2*$^{-/-}$ (compared to *5xFAD*). Genes were ranked by FC of 8-month-old

5xFAD;TREM2$^{-/-}$ versus *5xFAD*; samples were grouped by genotype and time point (*5xFAD*: n=14M/14F, *5xFAD;TREM2*$^{-/-}$: n=11M/11F at 4 months; and *5xFAD*: n=10M/9F, *5xFAD;TREM2*$^{-/-}$: n=9M/8F mice at 8 months). (C) Volcano plot of *5xFAD;CD33*$^{-/-}$ microglia versus *5xFAD* at 8 months revealed 8 downregulated ($log_2FC<-1$, FDR<0.05, blue) and 274 upregulated ($log_2FC>1$, FDR<0.05, red) genes. (D) Volcano plot of 8-month-old *5xFAD;TREM2*$^{-/-}$ microglia versus *5xFAD*. (E) Gene set enrichment analysis revealed 277 gene sets enriched for *5xFAD;CD33*$^{-/-}$ versus *5xFAD* and 342 gene sets for *5xFAD;TREM2*$^{-/-}$ versus *5xFAD* group (p-value<0.001, FDR<0.05) at 8 months. The top 30 significant gene sets are shown for each group. (F) Enrichment maps were generated for 8-month-old *5xFAD;CD33*$^{-/-}$ versus *5xFAD* and *5xFAD;TREM2*$^{-/-}$ versus *5xFAD* datasets. Four edges (connections) were found between the gene sets related to the extracellular collagen matrix and chemokine receptor activity cluster. See also Figures S7, S8 and Tables S2 and S5.